

# Rational design of nanoscale stabilized oxide catalysts for OER with OC22

Richard Tran,<sup>\*,†,‡</sup> Liqiang Huang,<sup>†,¶</sup> Yuan Zi,<sup>¶</sup> Shengguang Wang,<sup>‡</sup> Benjamin M. Comer,<sup>§</sup> Xuqing Wu,<sup>||</sup> Stefan J. Raaijman,<sup>⊥</sup> Nishant K. Sinha,<sup>#</sup> Sajanikumari Sadasivan,<sup>#</sup> Shibin Thundiyil,<sup>#</sup> Kuldeep B. Mamtani,<sup>#</sup> Ganesh Iyer,<sup>#</sup> Lars Grabow,<sup>§,‡</sup> Ligang Lu,<sup>\*,§</sup> and Jiefu Chen<sup>\*,¶</sup>

<sup>†</sup>Indicates equal contributions

<sup>‡</sup> *William A. Brookshire Department of Chemical and Biomolecular Engineering and Texas Center for Superconductivity (TcSUH), University of Houston, 4226 Martin Luther King Boulevard, Houston, TX 77204, USA.*

<sup>¶</sup> *Department of Electrical and Computer Engineering, University of Houston, 4226 Martin Luther King Boulevard, Houston, TX 77204, USA.*

<sup>§</sup> *Shell Global Solutions, Houston, TX 77082, USA.*

<sup>||</sup> *Department of Information Science Technology, University of Houston, 14004 University Boulevard #318, Sugar Land, TX 77479, USA.*

<sup>⊥</sup> *Energy Transition Campus Amsterdam, Shell Global Solutions International B.V. Grasweg 31, 1031 HW Amsterdam, the Netherlands.*

<sup>#</sup> *Shell Technical Center Bangalore, 7, Bengaluru Hardware Park KIADB Industrial Park North, Mahadeva Kodigehalli, Bengaluru, Bangalore, Karnataka 562149, India.*

E-mail: rtran17@uh.edu; ligang.lu@shell.com; jchen84@uh.edu

## Abstract

The efficiency of H<sub>2</sub> production via water electrolysis is typically limited to the sluggish oxygen evolution reaction (OER). As such, significant emphasis has been placed upon improving the rate of OER through the anode catalyst. More recently, the Open Catalyst 2022 (OC22) framework has provided a large dataset of density functional theory (DFT) calculations for OER intermediates on the surfaces of oxides. When coupled with state-of-the-art graph neural network models, total energy predictions can be achieved with a mean absolute error as low as 0.22 eV. In this work, we interpolated a database of the total energy predictions for all slabs and OER surface intermediates for 4,119 oxide materials in the original OC22 dataset using pre-trained models from the OC22 framework. This database includes all terminations of all facets up to a maximum Miller index of 1. To demonstrate the full utility of this database, we constructed a flexible screening framework to identify viable candidate anode catalysts for OER under varying reaction conditions for bulk, surface, and nanoscale Pourbaix stability as well as material cost, overpotential, and metastability. From our assessment, we were able to identify 122 and 68 viable candidates for OER under the bulk and nanoscale regime respectively.

## Keywords

Catalysis, oxides, renewable energy, datasets, machine learning, high-throughput screening, nanoscale stability

# 1 Introduction

As the global focus shifts increasingly towards renewable energy, there has been a significant rise in the demand for cost-effective and environmentally sustainable energy storage and transmission methods. Electrochemical water splitting, or water electrolysis, is a sustainable and promising means of evolving  $H_2$  thanks to the wide abundance of water. This process involves two coupled half-reactions: hydrogen evolution reaction (HER) and the significantly slower oxygen evolution reaction (OER) which has primarily been the bottleneck in advancing water-splitting technology. The search for a highly active anode catalyst for OER is therefore paramount to the realization of practical water splitting technology.<sup>1-4</sup>

Transition metal oxides are a promising class of catalysts for OER due to their varying oxidation states for more efficient multi-electron transfer, stability under highly acidic conditions favorable towards OER, and active undercoordinated transition metals sites. In regard to commercialized catalysts,  $IrO_2$  and  $RuO_2$  are the benchmark catalysts for OER, exhibiting low overpotentials (an indicator of activity) of 0.25 to 0.5 V under acidic conditions.<sup>5</sup> However, the material cost of precious metals (\$18,315 and \$155,727 per kg for  $RuO_2$  and  $IrO_2$  respectively as of March 2021<sup>6-8</sup> with a price variation of  $\pm$  \$9,969 for  $RuO_2$  and + \$80,370 for  $IrO_2$  in the last 24 years) limits their widespread adoption. Consequently, there is much desire to identify cheaper materials for catalysts in OER while maintaining similar performance.

Despite the abundance of unary and binary oxides, very few are capable of exhibiting both high catalytic activity and stability under operating conditions. Computational analysis performed by Wang et al.<sup>9</sup> indicated only 68 bimetallic oxides from a pool of 47,814 were stable with a Pourbaix decomposition energy ( $\Delta G_{PBX}$ ) of 0.5 eV/atom or less under acidic conditions (pH=0) and an applied potential cycle between 1.2 and 2.0 V. Gunasooriya and Nørskov<sup>10</sup> calculated the overpotential of these candidate oxides and identified only 11

nonbinary metal oxides with a promising overpotential of less than 0.85 V.

It is possible that many materials filtered out by the highly discriminant electrochemical stability criteria can also exhibit competitive overpotentials if stabilized. Nanoscale stability, elemental doping, and the introduction of oxygen vacancies have been demonstrated to be effective means of improving stability.<sup>1,11,12</sup> Nanoscaling in particular presents a promising avenue for stabilizing oxides under operating conditions while exposing a greater number of active sites through the increasing surface area-to-volume ratio (SA:V).<sup>13-15</sup>

However, an accurate evaluation of the nanoparticle formation energy not only requires the thermodynamic contributions of the bulk, but the surface as well. Doing so requires an ensemble of expensive Density Functional Theory (DFT) calculations of the bare surfaces for one material. Likewise, accurate evaluations of the overpotential requires an even larger set of calculations for all the surface intermediates participating in OER. As such, doing so for the massive pool of binary and unary oxide materials available will quickly become computationally expensive and unfeasible.

Machine learning (ML) potentials and screening frameworks have recently contributed significantly in rapidly predicting candidate catalysts without the need for expensive systematic DFT screening.<sup>16-20</sup> Among these efforts, the Open Catalyst Project (OCP)<sup>21</sup> framework has stood out as having the largest dataset of carefully curated DFT calculations for non-oxide slabs and surface intermediates to-date. ML models pre-trained with the OCP has allowed for large scale interpolation efforts to predict binding energies, enabling high-throughput screening efforts to identify viable catalyst candidates<sup>22</sup> and explore fundamental surface chemistry.<sup>23</sup> More recently, the Open Catalyst 2022 (OC22) framework has expanded upon this dataset by incorporating random combinations of 4,728 oxide materials, Miller indices up to 3, and surface intermediates involved in OER.<sup>24</sup> These efforts have yielded predictive ML models with total energy mean

absolute error (MAE)s of less than 0.22 and 0.69 eV for *in domain* (materials observed during training) and *out of domain* predictions, respectively.

In this manuscript, we utilized a pre-trained model from the OC22 framework to interpolate the surface energies and OER binding energies for 4,119 *in domain* oxide materials on all facets up to a maximum Miller index (MMI) of 1. To demonstrate the applicability of our interpolated database, we constructed a high-throughput screening framework with a set of progressive criteria that can be modified or expanded upon for ease of customizeability in order to evaluate the commercial and practical viability of each material for OER. Our general framework evaluates materials based on thermodynamic stability, overpotential, and material cost. We also expand upon other screening criteria such as the possibility of nanoscale stabilization or the faceting of surfaces on the equilibrium crystal structure. We propose 190 possible candidates for OER under the bulk and nanoscale regime respectively that warrant further experimental investigation.

## 2 Methods

All analysis were performed using the python materials genomics (*pymatgen*)<sup>25-28</sup> and Atomic Simulation Environment (ASE)<sup>29</sup> packages.

### 2.1 Slab generation

We described all facets up to a MMI of 1 containing an atomic and vacuum layer of 12.5 Å thick. The bulk materials used for slab construction in this study were obtained from the Materials Project.<sup>30</sup> We also considered all terminations for each facet (*sans* slabs exceeding 200 atoms) while maintaining equivalent surfaces on both sides of the slab which consequently resulted in non-stoichiometric slabs with respect to the bulk formula. Although the original OC22 dataset covered 4,732 distinct bulk oxide materials, the conventional unit cell of some of these materials contains over 100 atoms making the construction of

slabs exceed our 200 atom limit for the majority of facets considered. As such, we limit our study to slabs constructed from unit cells of less than 100 atoms. Furthermore, slabs constructed from a select number of materials resulted in the forces in the ML model being unconverged. Thus, we omitted 609 from the original 4,732 materials in the OC22 dataset that exhibited these behaviors, with our final bulk set containing 3,823 binary (A-B-O) and 296 unary (A-O) oxides. For all slabs constructed, we modelled the surface intermediates of O\*, OH\*, and OOH\*. To avoid periodic interactions between the adsorbates, all slabs were expanded along the length and width to at least 8 Å. We assumed all adsorbates bind through the O atom on available undercoordinated metal sites. All bare surface and surface intermediate models were constructed using the python framework adapted from OC22<sup>24,31,32</sup>.

### 2.2 DFT and machine learning settings

All DFT calculations were performed using the Vienna *Ab Initio* Simulation Package (VASP)<sup>33-36</sup> within the Projected Augmented Wave (PAW)<sup>37</sup> approach. We modeled the exchange-correlation effects with the Perdew-Berke-Ernzerhof (PBE) generalized gradient approximation (GGA) functional.<sup>38</sup> All calculations were performed with spin-polarization with a plane wave energy cut-off of 500 eV. The energies and atomic forces of all calculations were converged to within  $1 \times 10^{-4}$  eV and  $0.05 \text{ eV \AA}^{-1}$ , respectively. We used  $\Gamma$ -centered k-point meshes of  $\frac{30}{a} \times \frac{30}{b} \times 1$  for slab calculations, with non-integer values rounded up to the nearest integer. We also apply a Hubbard U correction to chemical systems as suggested by the Materials Project<sup>39</sup> to account for missing electron interactions.

We used a pre-trained model for the *Structure to Energy and Forces* (S2EF)-*Total* task from the OC22 framework to perform all machine learning predictions of the relaxed structure and total energy. The entirety of the Open Catalyst 2020 (OC20) dataset (1,281,040 DFT relaxations) was used to train an S2EF-*Total*

model which was subsequently fine-tuned with the OC22 dataset (62,331 DFT relaxations) to better predict the total energies of oxide surfaces and surface intermediates. The model was trained using the GemNet-OC architecture<sup>40</sup> due to its superior performance in energy predictions when compared to other graph neural network (GNN) architectures as a consequence of its improved capturing of long-range and quadruplet interactions.

For further details regarding additional parameters used in VASP or the construction of the machine learning model, we refer the reader to Tran et al.<sup>24</sup>.

All OC22 S2EF predictions and DFT calculations of slabs were performed with selective dynamics. In regards to surface energy predictions, both the bottom most and topmost layer of atoms within 1.25 Å were allowed to relax in the bare slab in order to ensure both surfaces had equal surface energy contributions. For the adsorption energies, only the topmost layer of atoms within 1.25 Å and any adsorbates were allowed to relax in the bare slab and surface intermediates. To avoid inadvertent desorption and dissociation of adsorbates during our ML relaxation, we applied a spring constant of 7.5 eV Å<sup>-2</sup> between all adsorbate atoms to preserve the identity of the molecule and between the adsorbate and host surface atoms whenever the adsorbate drifts 2 Å away from its initial position along the axis perpendicular to the surface.<sup>41,42</sup> Similarly, we also applied the same restorative force to all surface atoms when the relaxed trajectory exceeds 1 Å from the initial position of the ions to avoid drastic surface reconstruction. While this approach yields better interpretability for relaxed adsorption geometries, we recognize the inherent artificiality of these constraints and acknowledge the potential for desorption and dissociation. Consequently, we further implemented ML relaxation without such constraints on relaxed geometries exhibiting low overpotentials to verify the absence of desorption and dissociation phenomena. All values of overpotentials and Gibbs free energies reported in the main manuscript as well as Tables S1-S14 are relaxed without these ad-

ditional constraints unless stated otherwise. Comparisons of the overpotential and Gibbs free energy obtained with and without these constraints can be found in the ESI.

### 2.3 Surface thermodynamics

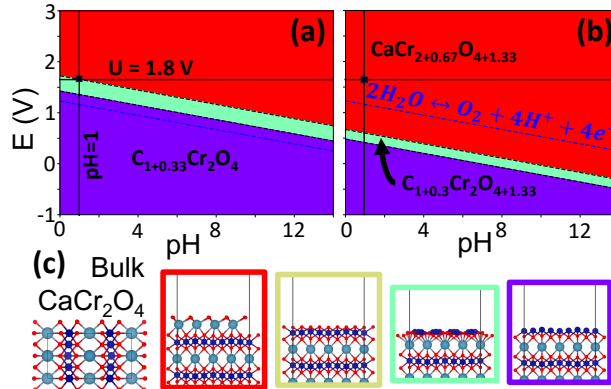


Figure 1: Surface Pourbaix diagram of the (001) facet of  $\text{CaCr}_2\text{O}_4$  at  $T = 80^\circ\text{C}$  under  $\Delta\mu_{\text{Cr}} = -4$  eV (a) and  $\Delta\mu_{\text{Cr}} = 0$  eV (b). The blue dashed line indicates the equilibrium conditions for OER while the black box indicates the desired conditions for OER ( $p\text{H} = 1$  and  $U = 1.8$  V). The phases in (a) and (b) are color coded with the corresponding terminations of the (001) facet in (c).

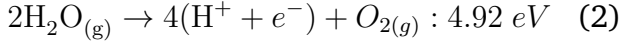
All bare slabs of formula  $\text{A}_{n_x}\text{B}_{n_y+k}\text{O}_{n_z+j}$ , with A and B being two metal components, are constructed from a bulk ternary oxide of  $\text{A}_x\text{B}_y\text{O}_z$ . We can calculate the surface energy of any slab of  $\text{A}_{n_x}\text{B}_{n_y+k}\text{O}_{n_z+j}$  with the following:

$$\gamma(\mu_B, \mu_{\text{O}_2}) = \frac{E_{slab}^{\text{A}_{n_x}\text{B}_{n_y+k}\text{O}_{n_z+j}} - (nE_{bulk}^{\text{A}_x\text{B}_y\text{O}_z} + k\mu_B + j\frac{1}{2}\mu_{\text{O}_2})}{2A} \quad (1)$$

where  $E_{slab}^{\text{A}_{n_x}\text{B}_{n_y+k}\text{O}_{n_z+j}}$  is the total energy of the bare slab,  $E_{bulk}^{\text{A}_x\text{B}_y\text{O}_z}$  is the total energy per formula unit of the bulk crystal, and  $A$  is the surface area. We used correction values from the Materials Project when evaluating  $\gamma$  to account for the mixing of quantities determined with GGA and GGA+U.<sup>26,39,43</sup> The chemical potentials,  $\mu_i$ , accounts for any nonstoichiometric species (with respect to bulk stoichiom-

etry) in the slab formula.

The chemical potential of oxygen ( $\Delta\mu_{O_2}$ ) can be referenced to the electrochemical decomposition of water to  $O_{2(g)}$ :



which allows us to rewrite  $\mu_{O_2}$  (and thereby  $\gamma$ ) as a function of  $pH$  and applied potential ( $U$ ) as such:

$$\begin{aligned} \Delta\mu_{O_2} = & \\ & 4.92 + 2\mu_{H_2O}^o - \\ & 4\left(\frac{1}{2}\mu_{H_2}^o - eU - k_B T pH \ln 10\right) + \Delta G_{corr}^{O*} \end{aligned} \quad (3)$$

where  $\Delta G_{corr}^{O*}$  corrects for the Gibbs free energy of excess or deficient oxygen at the surface (see Tran et al.<sup>24</sup> and Gunasooriya and Nørskov<sup>10</sup> for details). We will assume typically employed operating conditions for acidic OER ( $pH = 1$  and  $U = 1.8 \text{ V}$  at  $T = 80 \text{ }^\circ\text{C}$  or  $60 \text{ }^\circ\text{C}$ )<sup>9,44</sup> ( $\Delta\mu_{O_2} = -1.30 \text{ eV}$ ) when assessing the surface energy of all materials as illustrated in Figure 1(a and b). For slabs containing excess or deficient metal (B) species, the chemical potential of component B is conventionally referenced with respect to the per atom energy of the ground state bulk crystal of pure component B (e.g.  $\mu_{Fe} = \Delta\mu_{Fe} + E_{BCC,Fe}^{DFT}$ ). By varying the chemical potential of component B, we can stabilize different surface terminations of the same facet as shown in the surface Pourbaix diagram in Figure 1(a and b).

To determine the nanoscale stability of metastable and unstable materials under operating conditions, we assessed the nanoparticle formation energy given by:

$$\begin{aligned} G_f^{NP} = & \\ & E_V(pH, V, T) \left(\frac{4}{3}\pi r^3\right) + \bar{\gamma}(pH, V, T, \Delta\mu_M) (4\pi r^2) \end{aligned} \quad (4)$$

whereby  $E_V$  is the Pourbaix formation energy per volume of the unit cell,  $\bar{\gamma}$  is the weighted surface energy of the Wulff shape (an analogue to the nanoparticle morphology), and

$r$  is the radius of the nanoparticle. Detailed explanation of these quantities can be found in the ESI. Figure 2 demonstrates how a less stable compound ( $CaTi_2O_5$ ) can become more stable than the ground state compound as nanoparticle size and  $\Delta\mu_{Ti}$  decreases. The size effect will change the relative contribution of surface energy and bulk Pourbaix formation energy to  $G_f^{NP}$  while  $\Delta\mu_{Ti}$  changes the overall particle morphology and thereby surface energy of the particle.

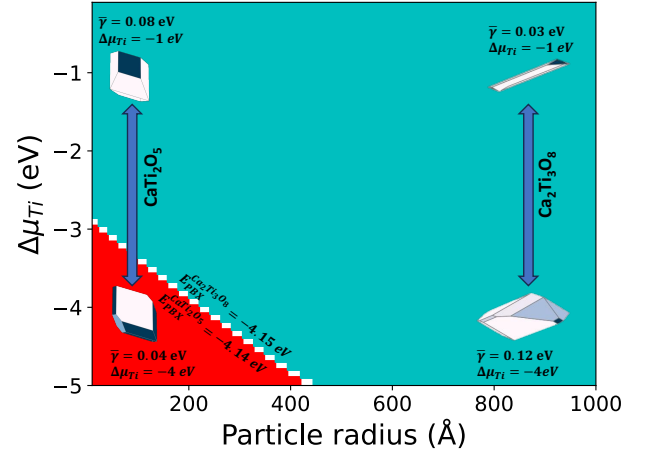


Figure 2: Nanoscale stability phase diagram for the Ca-Ti-O chemical system plotted using  $G_f^{NP}$  as a function of the chemical potential of Ti ( $\Delta\mu_{Ti}$ ) and nanoparticle radius. The red region represents the less stable (higher  $E_{PBX}$ ) phase ( $CaTi_2O_5$ ) while the cyan region represents the ground state phase ( $Ca_2Ti_3O_8$ ). The nanoparticle morphology and surface energy change as a function of  $\Delta\mu_{Ti}$  indicated by the inset Wulff shapes.

The scope of this study will explore the water nucleophilic attack (WNA) mechanism for OER, a four step mechanism where two water molecules sequentially bind to a metal at the surface and release an electron-proton pair at each step as shown in Figure 3.<sup>45</sup> We realize and emphasize that the WNA mechanism is one of many approximations for modeling OER and that it is possible for certain materials to prefer alternative mechanisms e.g. the oxo-coupling mechanism or lattice oxygen evolution reaction.<sup>46-50</sup> However, we focus on the WNA mechanism on account of

its ubiquity in computational studies<sup>51–55</sup> and supporting experimental evidence.<sup>47,56</sup> We can determine the overpotential for this reaction by identifying the largest energy difference between each step, reaction energy ( $\Delta G_{rxn}$ ) with the following:

$$\eta = \max(\Delta G^i, \Delta G^{ii} - \Delta G^i, \Delta G^{iii} - \Delta G^{ii}, 4.92 - \Delta G^{iii})/e - 1.23V \quad (5)$$

where  $\Delta G^i$ ,  $\Delta G^{ii}$ , and  $\Delta G^{iii}$  are the Gibbs free energy of each reaction step, 4.92 eV is the Gibbs free energy to dissociate two water molecules into  $O_2$  and  $4(H^+ + e^-)$  shown in Equation 2, and 1.23 V is the equilibrium potential for water decomposition. Here, the step corresponding to the largest value of  $\Delta G_{rxn}$  is also called the potential determining step (PDS). We can derive the Gibbs free energy of each step listed in Equations  $i - iv$  (see Figure 3) as such:

$$\Delta G^i = E_{ads}^{OH^*} + \Delta G_{corr}^{OH^*} + \mu_{H^+} + \mu_{e^-} \quad (6)$$

$$\Delta G^{ii} = E^{O^*} + \Delta G_{corr}^{O^*} + 2(\mu_{H^+} + \mu_{e^-}) \quad (7)$$

$$\Delta G^{iii} = E_{ads}^{OOH^*} + \Delta G_{corr}^{OOH^*} + 3(\mu_{H^+} + \mu_{e^-}) \quad (8)$$

where  $E_{ads}^{OH^*}$ ,  $E_{ads}^{O^*}$ , and  $E_{ads}^{OOH^*}$  are the electronic adsorption energies of the intermediates for OER and  $G_{corr}^{OH^*}$ ,  $G_{corr}^{O^*}$ , and  $G_{corr}^{OOH^*}$  are correction terms for the Gibbs free energy derived in the ESI of OC22.<sup>24</sup>

To minimize the number of predictions needed, we will begin by using a quick scaling relationship given by  $\Delta G^{iii} = \Delta G^i + 3.26$ <sup>10,24</sup> to estimate  $\Delta G^{iii}$ . This approach is particularly beneficial for  $OOH^*$ , where the significantly greater rotational freedom leads to a substantial increase in potential adsorbate placements. We will then perform additional predictions for  $E_{ads}^{OOH^*}$  for surfaces exhibiting promising activity ( $\eta < 0.75$  V) using Equation 8 to more accurately determine overpotential. ML relaxations exhibiting dissociation or desorption of intermediates are omitted in any interpretation of  $\eta$ . More details regarding dissociation and desorption events occurring

in the dataset as well as a comparison between  $\eta$  obtained with Equation 8 and scaling relationships can be found in the ESI.

Only the most stable site for  $OH^*$  dictated by  $E_{ads}^{OH^*}$  from a set of considered adsorption sites on the same surface is considered when determining  $\eta$ . We maintain the adsorption site corresponding to the most stable site of  $OH^*$  when considering  $E_{ads}^{O^*}$  and  $E_{ads}^{OOH^*}$ .

Further details regarding the derivation of all thermodynamic quantities and scaling relationships can be found in the ESI.

## 3 Results and Discussion

### 3.1 Database scope and usage

We emphasize that the purpose of both the OC20 and OC22 datasets was to establish a large and diverse set of DFT calculated surfaces and surface intermediates for the purpose of training ML potentials generalized to infer the total DFT of any slab and adsorbate combination. To maximize the diversity of the sample set, the OCP curated DFT calculations of randomly selected combinations of materials, surfaces, and adsorbates. The scope of the dataset **does not** encompass a comprehensive database for evaluating  $\eta$  directly, as many necessary data points are missing illustrated in Figure 4. The construction of a comprehensive database is a herculean task that is immeasurably costly and time consuming with DFT alone. However, by consolidating the S2EF-*total* model to predict thermodynamic overpotentials, we can potentially infer the catalytic activity of large material datasets for OER within a reasonable degree of error with respect to DFT.

Using the previously developed ML models, we systematically extrapolated the total DFT energy of all terminations for all facets up to a MMI=1 for all 4,119 materials considered in this study. We emphasize that although the original training pool does consider selections of bare and adsorbed surfaces up to MMI=3, the complete dataset is biased towards facets with a MMI=1 with 39,573, 15,482, and 7,276 data points of MMI=1, 2 and 3 respectively. We expect this bias to allow

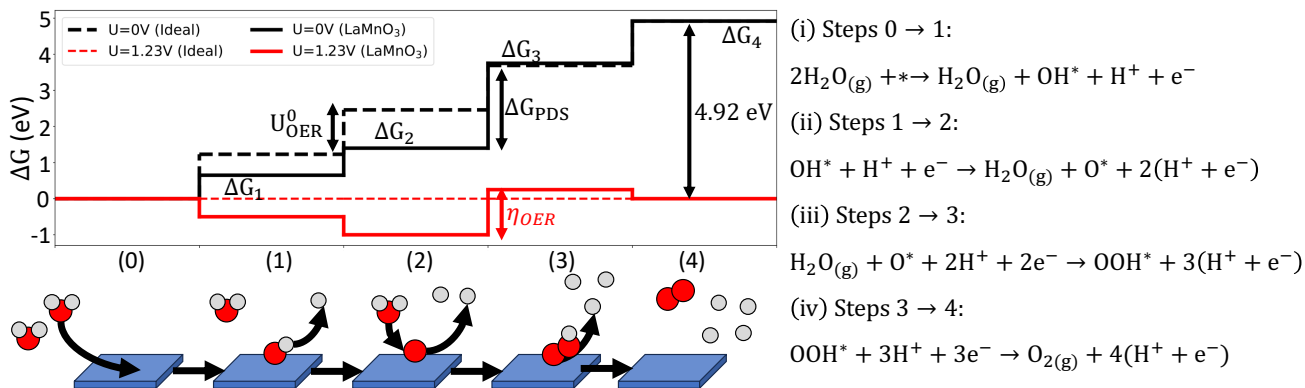


Figure 3: Reaction diagram for the WNA on an ideal catalyst (dashed lines) and  $\text{LaMnO}_3$  (100) surface (solid lines) at 0 V (black) and the equilibrium potential of OER (red). An illustration of each reaction step is shown at the bottom (red circles are oxygen while grey circles are hydrogen/protons). Reaction energies for  $\text{LaMnO}_3$  were derived from Man et al.<sup>45</sup>. The chemical equation between each reaction step (1-4) is listed on the right (i-iv).

for better predictions of the facets (all of which exhibit  $\text{MMI}=1$ ) considered in this work. We then extrapolated the total energy of all metal adsorption sites on all surfaces for  $\text{O}^*$  and  $\text{OH}^*$  (and  $\text{OOH}^*$  when  $\eta < 0.75$  V). Table 1 summarizes the scope of our extrapolated database. In contrast to our interpolation efforts, the size of the OC22 dataset for  $\text{O}^*$  and  $\text{OH}^*$  is only 0.1% of the predicted dataset in this work. Despite requiring orders of magnitude less computational resources than a DFT dataset of the same size, the estimated cost to produce our dataset is still 9,473.9 GPU-hrs. (an average rate of one prediction every 12.5 seconds), a significant amount of resources. By making this database freely available to the scientific community, users interested in performing similar high-throughput screening exercise or fundamental analysis can do so without the enormous cost in GPUs. The entire database including the initial and relaxed structures and total energies can be accessed through the University of Houston Dataverse Repository.<sup>57</sup> Details regarding the database metadata are given in the ESI.

For the 12,922 surfaces exhibiting  $\eta < 0.75$  V, we performed an additional ML relaxation step without the application of constraints on surface relaxation, adsorbate dissociation, and desorption. While only 7% of  $\text{OH}^*$  and 1% of  $\text{O}^*$  intermediates exhibited dissociation and

desorption event, an overwhelming number of events (50%) were associated with the  $\text{OOH}^*$  intermediates. Consequently, predictions of  $\eta$  exhibiting these events could not be interpreted and were ignored in our final assessment of overpotential. However, we emphasize that the occurrence of dissociation and desorption does not disqualify the possibility of these surfaces being catalytically active in alternative reaction mechanisms such as the oxo-coupling mechanism or lattice oxygen evolution reaction.<sup>46-50</sup>

Table 1: Summary of database scope

<b>Predictions: 6,068,572</b>			
<b>Materials: 4,119</b>			
<b>Ave. # slabs per material: 47</b>			
<b><math>\text{OH}^*</math></b>	<b><math>\text{O}^*</math></b>	<b><math>\text{OOH}^*</math></b>	<b>*</b>
1,972,166	667,266	3,237,238	191,902
<b>Predictions w/o spring constraints</b>			
<b>Predictions of <math>\eta</math>: 12,922</b>			
<b>Dissociation/desorption events</b>			
<b><math>\text{OH}^*</math></b>	<b><math>\text{O}^*</math></b>	<b><math>\text{OOH}^*</math></b>	
908	131	6,296	
<b>Predictions of <math>\eta</math> w/o diss./des. events: 6,468</b>			

## 3.2 High-throughput screening

Figure 5 summarizes the selection criteria that we employed to screen for candidate electrocatalysts for OER. The first criterion in our high-throughput screening framework was to



Figure 4: Scope of surface intermediates for OER calculated using DFT in the OC22 dataset. Overlaps indicate the number of surfaces where different intermediates ( $\text{OH}^*$ ,  $\text{O}^*$ , or  $\text{OOH}^*$ ) are calculated for the same surface.

determine if a material exists in the original training dataset of OC22. As previously demonstrated by Tran et al.<sup>24</sup>, the OC22 framework is capable of predicting the total DFT energies of slabs and surface intermediates of oxides within a mean absolute error of 0.22 eV for 4,119 materials that have been observed in the training dataset. Our database will only interpolate the energies of slabs and surface intermediates amongst these materials (for more information, the reader is redirected to<sup>24</sup>).

The second criterion describes the Pourbaix stability, i.e., the electrochemical stability of a material in an aqueous environment. Here, we can interpret Pourbaix stability under a bulk regime (right side of Figure 5). We quantify the Pourbaix stability of the bulk using the Pourbaix decomposition energy ( $E_{PBX}$ ), which is a function of the temperature (T) applied potential (U) and pH of the environment (at T = 80°C, U = 1.8 V, and pH = 1).<sup>27,28</sup> Materials with  $E_{PBX} = 0$  eV per atom are stable under such conditions while materials with  $E_{PBX} > 0$  eV atom<sup>-1</sup> are metastable with the

likelihood of corrosion increasing with  $E_{PBX}$ . It was shown experimentally that metastable materials with  $E_{PBX} \leq 0.2$  eV per atom are less likely to dissolve or corrode.<sup>58</sup> However, materials with  $E_{PBX}$  as high as 0.5 eV atom<sup>-1</sup> have also been shown to be stable, albeit with a degree of surface passivation which can inhibit catalytic activity.<sup>27</sup> We allow any material with  $E_{PBX} \leq 0.5$  eV per atom under the aforementioned conditions (see Figure 1)(a) to satisfy this criterion. Due to the exclusive nature of  $E_{PBX}$ , only 1,853 of the original 4,119 materials will satisfy this criterion.

We adapted our third selection criterion based on the selection criterion from the WhereWulff<sup>59</sup> high-throughput screening workflow for oxide catalyst discovery. Here, we assess the surface energy of every termination for each facet of each material that is Pourbaix stable with Equation 1. From the surface energy, we were able to construct the Wulff shape which indicates the most prominent facets in an equilibrium crystal. When considering which surfaces are stable and can potentially facilitate OER, we only consider surfaces that appear on the Wulff shape. Depending on the stoichiometry of the slab, the surface energy can vary as a function of  $\Delta\mu_M$ . For simplicity, we will roughly assume a possible chemical potential range of the metal M as  $-5 < \Delta\mu_M < 0$  eV when interpreting surface energy. Wulff shapes containing negative surface energies are ignored as nonphysical solutions as this indicates the surface is more stable than the bulk (which implies dissolution of the solid). The dissolution of the Wulff shape will consequently lead to 314 additional materials being omitted from our list of candidates, leaving us with 1,539 materials with 11,918 stable surfaces on the Wulff shape.

In our fourth criterion, we assess the overpotential of each candidate surface with Equation 5. We consider any material with at least two facets on the Wulff shape exhibiting  $\eta < 0.75$  V as being potentially competitive with  $\text{RuO}_2$  and  $\text{IrO}_2$  in regards to catalytic performance. We find that 101 materials (512 surfaces) from our previous 1,539 materials will satisfy this criterion.



The fifth criterion assesses the thermodynamic stability of the candidate material via the energy above hull ( $E_{hull}$ ) or the formation energy of a material relative to the ground state. Like with Pourbaix stability, materials with a calculated  $E_{hull} > 0$  eV per atom are metastable with the likelihood of experimental synthesizability decreasing as  $E_{hull}$  increases. Materials with a calculated  $E_{hull} \leq 0.1$  eV per atom have been shown to have reasonable rates of demonstrated synthesis in experiment.<sup>60</sup> From our aforementioned 101 catalytically active candidates, we identify 92 materials that are metastable.

The final criterion assesses the material cost of each compound in \$ per kg. To satisfy this criteria, the cost of a compound must be less than that of RuO<sub>2</sub> or \$18,315 per kg (as of March 2021<sup>6-8</sup>). As a conservative estimate, we will also assume a price variation of \$9,969/kg (based on the lowest and highest prices of Ru in the last 24 years) in the future and as such, all materials must be less than \$8,346/kg. We have identified 81 materials and 66 distinct chemical systems from our 101 metastable materials that have satisfied this criterion. A tabulated list of all candidates with the lowest value of  $\eta$ ,  $E_{hull}$ ,  $E_{PBX}$ , material cost, space group, and number of facets with low overpotentials is give in Table S1-S8.

### 3.3 Overpotential assessment

Although our set of tiered screening criteria will provide the most economically and industrially viable candidates with respect to thermodynamic stability and material cost, we posit that there is a wider range of materials that can have competitive overpotentials necessary for OER when ignoring the criteria listed above. Figure 6(a) shows the 53 elements on the periodic table considered in our database. The heatmap indicates the number of materials containing an element that exhibits at least 2 facets with  $\eta < 0.75$  V. Oxide combinations containing Cr, Mn, Co, Cu, Bi, Pb, Se, Tl, Ag, and Sb tend to form catalysts that exhibit low overpotentials. Ag-based chemical systems such as Ag-O,<sup>61</sup> Ag-Bi-O,<sup>62</sup> Ag-Cu-O,<sup>63</sup> and Ag-Co-O<sup>64</sup> have been

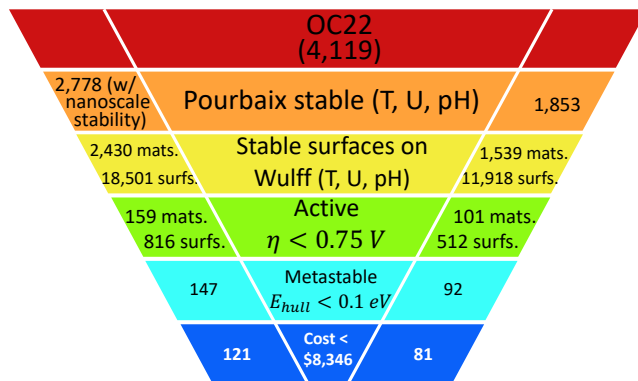


Figure 5: Summary of the screening criteria considered in our high-throughput screening framework. The possible number of candidates that have satisfied each tier is listed on the right for bulk Pourbaix stable materials and on the left when nanoscale stability is possible. The second and third criteria can be further modified by changing the environmental parameters (T, U, pH).

demonstrated as viable catalysts for OER in experimental settings. The common use of Ag has been attributed to the fact that Ag has the highest electrical conductivity amongst all metals, allowing it to easily facilitate the four electron charge transfer process that takes place during OER.<sup>64</sup> Although it is not as common and cheap as the 3d transition metals, Ag is still more reasonably priced than the other noble metals. Furthermore, it has been shown that Ag-doping at 1% has been enough to enhance charge transfer in OER,<sup>65</sup> making Ag-based oxides reasonably economical. Similarly, Mn-based chemical systems are known to be promising catalysts for OER. This is owed to the intrinsically high activity and number of polymorphs for compounds of MnO<sub>x</sub><sup>66</sup> which can be synergistically improved when introducing other components such as Fe,<sup>67</sup> Ni,<sup>68</sup> and Co.<sup>69</sup> Antimonates (Sb-based oxides) have been extensively studied in both computational<sup>10</sup> and experimental<sup>62,70-72</sup> settings as promising low-cost anode catalysts for OER owed to their low overpotential and high operational stability as a consequence of Sb-O p-d hybridisation.<sup>72</sup> Mixed metal Co oxides are abundant in CO<sup>2+</sup> cations that are use-

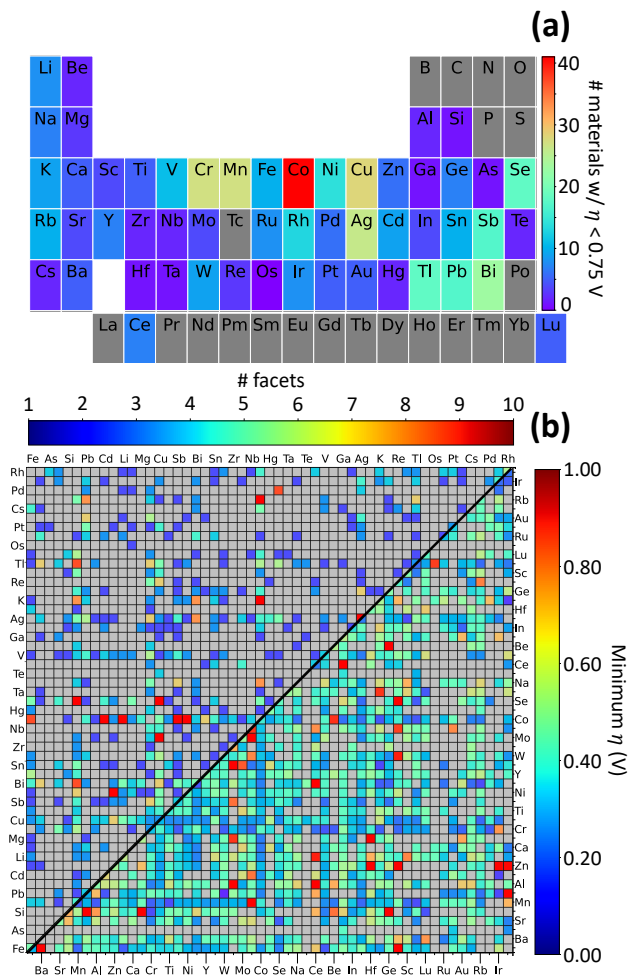


Figure 6: (a) Periodic table of elements considered in the database. Colormap indicates the number of materials containing the element that exhibit  $\eta < 0.75$  V for at least two facets. (b) Grid map for each pair of elements with colors indicating the lowest overpotential amongst all facets on the Wulff shape containing this chemical system (bottom right) and the number of facets on the Wulff shape across material with the same chemical system that exhibit overpotentials less than 0.75 eV (top left). Tick labels on the x- and y-axis are sorted from the cheapest (Fe) to the most expensive (Rh) element.

ful for OER. The large atomic difference between Co and the larger metal in Co-based Perovskites can also lead to distortions in the structure that can better stabilize either the  $\text{CO}^{2+}$  or  $\text{CO}^{3+}$  cation which can allow for tunable active sites.<sup>73</sup>

Non-noble chemical systems such as Fe-

Ni,<sup>74</sup> Cu-Fe, Fe-Mn,<sup>75</sup> Fe,<sup>76</sup> Co-Mn,<sup>77</sup> and Co-Cr<sup>78</sup> based oxides have been shown to exhibit competitive overpotentials in the experimental literature despite their absence from our final set of candidates. To account for this discrepancy, we predicted the overpotentials for all Wulff shape facets of all 4,119 materials. We summarized the overpotential of each chemical system by plotting the lowest overpotential and the number of facets exhibiting  $\eta < 0.75$  eV in Figure 6(b) across all materials of the same chemical system as a heat map. Upon further inspection, Fe-Mn-O is shown to be relatively unstable in our dataset ( $E_{P_{bx}} = 0.95$  eV) despite having a competitive overpotential corroborating with past experiments. However, this was explored in the context of nanoparticle catalysts<sup>75</sup>.

We have demonstrated 380 chemical systems exhibiting facets on the Wulff shape that are potentially active for OER despite only 76 chemical systems (92 materials) (ignoring material cost) appearing in our set of candidates due to the bulk stability of many materials being inaccessible. Methods for stabilizing bulk oxides such as nanoscale stability (e.g. in the aforementioned case for Fe-Mn-O<sup>75</sup>), elemental doping, and the introduction of oxygen vacancies have been demonstrated to be effective means of improving stability.<sup>1</sup>  $\text{RuO}_2$  for example is known to have stability issues in aqueous environments despite being the benchmark for OER catalysts. However doping with other metals such as Cr and Ti has been shown to stabilize this material.<sup>11</sup> With these methods of stabilizing the catalyst material and accessing active surfaces, we emphasize that the identification of viable catalysts should not strictly be confined by the Pourbaix stability or even  $E_{hull}$ . As an example, we will demonstrate how nanoscale stabilization can potentially expand the material space available for OER to access these materials.

### 3.4 Alternative screening frameworks

Table 2 shows the number of final candidates identified under different reaction conditions and definitions of Pourbaix stability. In this

Table 2: The different screening frameworks assessed in this study with varying reaction conditions and criteria for Pourbaix stability. All screening frameworks are assumed to occur under pH=1. Superscript letters are used to label each framework evaluated (see Table S1-S8 for a list of candidates that were identified in each framework). Numbers in parentheses correspond to conductive candidates with small band gaps ( $E_{gap} < 0.1$  eV) Framework  $j$  and  $k$  correspond to the frameworks investigated in Figure 5

Temperature ( $^{\circ}C$ )	60	60	80	80
Applied Potential (V)	1.8	1.2-2.0	1.8	1.2-2.0
Bulk	122 <sup>a</sup>	99 <sup>e</sup>	120 <sup>i</sup>	99 <sup>m</sup>
Bulk/Wulff	83 <sup>b</sup>	62 <sup>f</sup>	81 <sup>j</sup>	62 <sup>n</sup>
Bulk/Wulff/Nano	111 <sup>c</sup>	83 <sup>g</sup>	121 <sup>k</sup>	84 <sup>o</sup>
Bulk/Nano	168 <sup>d</sup>	129 <sup>h</sup>	181 <sup>l</sup>	129 <sup>p</sup>

study we constructed a database of machine learning data and demonstrated how it can be used in a variety of ways to screen for catalyst. First, we identified potential candidates for OER by creating a screening framework based on simple bulk thermodynamic (the energy above hull and Pourbaix energy above hull) and surface stability arguments at  $pH = 1$ ,  $U = 1.8$  V, and  $T = 80^{\circ}C$  (see  $j$  in Table 2). We can easily modify our framework to reflect other reaction conditions and criteria for Pourbaix stability as shown in Table 2. For example, we can modify our framework by introducing an additional layer of complexity to our definition of Pourbaix stability by analyzing the possibility of nanoscale stability under acidic conditions for OER as demonstrated in Figure 5 (right). Using our nanoscale stability diagrams (see Figure 2), we were able to identify 2,778 Pourbaix stable materials with 886 stabilizing at the nanoscale regime (10 to 100 nm). From our Wulff shape analysis of the 2,778 Pourbaix stable materials, we identified 18,501 surfaces that appear on the Wulff of 2,430 materials. We find that 816 of these surfaces (from 159 materials) also exhibit low overpotentials. From these 159 potentially active materials, 147 are metastable and 121 exhibit a material cost less than  $RuO_2$ . In total

we have identified 121 candidates and 40 additional candidates that are potentially commercially viable for OER when synthesized as nanoparticles (see  $k$  in Table 2).

Another example of how we can modify our screening framework is by changing our criteria for surface stability. As mentioned before, we only considered facets that appear on the Wulff shape within a metal chemical potential between  $-5 < \Delta\mu_M < 0$  eV. The Wulff shape indicates the most statistically likely facets to appear under equilibrium crystal growth conditions. However, non-equilibrium conditions can potentially force different types of facets to appear.<sup>79</sup> We can account for this in our screening framework by considering all facets as viable surfaces for OER. With this simple assumption, we identified 181 materials (120 and 61 in the bulk and nanoscale regime respectively) that satisfy all criteria (see  $l$  in Table 2). Among the chemical systems identified as nanostable is Fe-Mn-O which as mentioned previously, has been explored as nanoparticle catalysts for OER.<sup>75</sup>

Other alternative screening frameworks can be explored by simply adding or modifying existing criteria. As a simple example, we can assess Pourbaix stability under different temperature conditions. The operating temperatures for OER are typically between 60  $^{\circ}C$  and 80  $^{\circ}C$  with higher temperatures resulting in improved ionic conductivity and kinetics in exchange for lower stability. Although our assessment assumes an operating temperature of 80  $^{\circ}C$ , we can easily re-assess the second criteria (for bulk stability) in our screening framework at 60  $^{\circ}C$  instead which will yield 2 additional candidates without considering nanoscale stability ( $a$  and  $b$ ). When nanoscale stability is considered however, lowering the temperature from 80  $^{\circ}C$  to 60  $^{\circ}C$  will result in a loss of 10 ( $c$ ) and 13 ( $d$ ) candidates with and without Wulff shape stability respectively. The bulk Pourbaix formation energy of ground state polymorphs decreases at lower temperatures. This decreases the likelihood for metastable polymorphs to become more stable than the ground state at the nanoscale resulting in fewer nanostable candidates at

lower temperatures.

We can also consider more complex and realistic reaction conditions whereby candidates are assessed based on their stability over a range of operating potentials. We adopted the potential range of 1.2-2.0 V for OER for which a material must remain stable (or metastable with  $E_{PBX} \leq 0.5$  eV) as suggested by Wang et al.<sup>9</sup> ( $e-h$  at  $T = 60$  °C and  $m-p$  at  $T = 80$  °C). This strict set of operating conditions unsurprisingly results in fewer candidates when compared to a static potential operating condition of 1.8 V. The total number of candidates presented in this work however, still far exceeds the original set of candidates identified by Wang et al.<sup>9</sup> and subsequently proposed by Gunasooriya and Nørskov<sup>10</sup>. The OC22 framework is trained on data calculated with the PBE-GGA functional whereas the data presented by Wang et al.<sup>9</sup> was obtained using the more accurate SCAN functional<sup>80</sup> with the addition of correction terms better suited for assessing stability under corrosive conditions. These considerations contributed to a more realistic, albeit pessimistic, set of 17 Pourbaix stable and active candidates subsequently found by Gunasooriya and Nørskov<sup>10</sup> as oppose to the 99 bulk stable candidates identified at 80 °C ( $m$ ). In a future work, we hope to adapt these functionals and corrections when assessing nanostable catalysts to provide a more accurate expansion to the limited set of bulk stable candidates explored by the references herein<sup>9,10</sup>.

In total we have identified 190 candidates (122 bulk- and 68 nanostable) with 145 distinct chemical systems when considering all the different screening frameworks listed in Table 2. In the next section, we will validate our findings by comparing to past experimental and computational results as well as our own DFT simulations. We hope this demonstration regarding the ease and variability of how these frameworks can be modified illustrates the utility of these machine learning databases. We highly encourage the scientific community to use our database to explore further possibilities and alternative screening frameworks in the future.

### 3.5 DFT and literature validation

We used DFT to validate 85 values for Gibbs adsorption energy corresponding to Equations 6-8 for 33 Pourbaix stable compounds in our database. The MAE of the test set shown in Figure 7(a) is 0.42 which is larger than the MAE of 0.239 eV obtained from the validation set in the original OC22 assessment.<sup>24</sup> We find no difference in the amount of error when validating ML data points with (square) and without (circle) desorption/dissociation event. However, ML values corresponding to  $O^*$  adsorption on  $Ag_2SeO_3$  and  $Na_2Se_2O_7$  and  $OOH^*$  adsorption on  $Ag_2SeO_3$  will underestimate  $\Delta G_{ads}$  relative to DFT. These data points exhibit better agreement with DFT when applying a spring constant constraint to prevent dissociation/desorption events (transparent data points). This implies that the model from OC22 may overestimate the tendency for desorption/dissociation in some combinations of intermediates and surface and could be a potential point of improvement in future iterations of the model.

Next we assess the predictability of the ML inferred overpotential (Equation 5) using the predicted and calculated values of  $\Delta G_{ads}$  from Figure 7(a). Figure 7(b) once again plots the DFT calculated data points against the corresponding ML quantities. The majority of data points sampled will lie within the MAE of 0.22 V, however overpotentials corresponding to  $KSnO_2$ ,  $Na_5ReO_6$ ,  $Ag_2SeO_3$ , and  $Na_2Se_2O_7$  will lie outside the MAE.  $Ag_2SeO_3$  and  $Na_2Se_2O_7$  will exhibit overpotentials closer to parity with DFT when applying a spring constant constraint to prevent the dissociation/desorption of  $O^*$  and  $OOH^*$  in  $Ag_2SeO_3$  and  $O^*$  in  $Na_2Se_2O_7$  as shown in Figure 7(a). Despite the large deviation from MAE however, we find that most data points with predicted low overpotentials will still exhibit low overpotentials close to or less than 0.75 V using DFT with the exception of  $KSnO_2$  and  $Na_5ReO_6$ .

From our DFT calculations, we were able to identify 6 data points with overpotentials below the soft theoretical limit ( $\eta_{Th} > 0.3$  V) imposed by scaling relationships:  $Mn_{23}FeO_{32}$ ,

HgSeO<sub>4</sub>, Na<sub>2</sub>Co<sub>2</sub>O<sub>3</sub>, Cd<sub>2</sub>PbO<sub>4</sub>, MnTlO<sub>3</sub>, and KBiO<sub>2</sub>. The Mn-Fe-O chemical system is well explored in the literature with experimental overpotentials as low as 0.47 V.<sup>75,81,82</sup> Although no studies have investigated ordered structures of Na-Co-O, the doping of layered CoO<sub>2</sub> with Na has resulted in overpotentials as low as 0.24 V.<sup>83</sup> Although we have predicted HgSeO<sub>4</sub> and Cd<sub>2</sub>PbO<sub>4</sub> as having overpotentials less than  $\eta_{Th}$ , Pb, Cd, and Hg are known to possess potential health risks<sup>84</sup> and as such, caution is advised for any further investigation of candidates containing these elements. As far as we are aware, the Mn-Tl-O and Bi-K-O chemical systems have yet to be explored in the literature.

Lastly, we compared our predicted values of overpotential to those obtained by Gunasooriya and Nørskov<sup>10</sup> for various facets of 11 materials in Figure 7(b). The majority of our predicted datapoints lie within a MAE of 0.38 V. ML data points tend to underestimate the DFT values. However, those that lie well beyond 0.38 V, such as IrO<sub>2</sub>, Ni(SbO<sub>3</sub>)<sub>2</sub>, TiSnO<sub>4</sub>, Sn(WO<sub>4</sub>)<sub>2</sub>, Sn(WO<sub>4</sub>)<sub>2</sub>, FeSbO<sub>4</sub> will again exhibit overpotentials much closer to parity with DFT when applying a spring constant constraint to prevent the dissociation/desorption. A key difference in the methods used to obtain both datasets is that the surfaces observed by Gunasooriya and Nørskov<sup>10</sup> can be covered completely by O\* or OH\* whereas all surfaces considered in this study only considered the adsorption of a single O\* or OH\* intermediate at a time. Despite this, we still find many data points terminated by O\* or OH\* within the MAE.

Table S9-S14 lists all 190 candidate materials we have identified in this work along with references to the experimental literature where available and the PDS of the surface with the lowest overpotential. In total, we have identified 102 out of 145 unique chemical systems (127 out of 190 materials) that have yet to be explored with 77 non-toxic (does not contain Pb, Cd, Hg, or Cr) chemical systems (98 materials). Although not considered in our study, conductivity is also required for the operation of electrocatalysts.<sup>9</sup>

Of these 98 non-toxic and unexplored candidates, 27 have a band gap of less than 0.1 eV according to the Materials Project<sup>30</sup> which satisfies this additional criteria. These conductive candidates are: Cu<sub>3</sub>(SbO<sub>3</sub>)<sub>4</sub>, Ba<sub>8</sub>(Bi<sub>2</sub>O<sub>7</sub>)<sub>3</sub>, BaBiO<sub>3</sub>, Cu<sub>3</sub>Mo<sub>2</sub>O<sub>9</sub>, Mg(BiO<sub>3</sub>)<sub>2</sub>, CuMoO<sub>4</sub>, Li(Bi<sub>3</sub>O<sub>5</sub>)<sub>4</sub>, Ce<sub>2</sub>Mo<sub>4</sub>O<sub>15</sub>, Ce<sub>9</sub>YO<sub>20</sub>, AgSnO<sub>3</sub>, Ce<sub>2</sub>(GeO<sub>3</sub>)<sub>3</sub>, Ag<sub>4</sub>GeO<sub>4</sub>, MnTlO<sub>3</sub>, LuCoO<sub>3</sub>, BaMn<sub>2</sub>O<sub>3</sub>, Li(CuO)<sub>2</sub>, MnBiO<sub>3</sub>, Mn<sub>2</sub>BeO<sub>4</sub>, VZn<sub>2</sub>O<sub>4</sub>, ScMn<sub>2</sub>O<sub>4</sub>, LiMn<sub>3</sub>O<sub>4</sub>, Mn<sub>3</sub>NiO<sub>4</sub>, Mn<sub>2</sub>NiO<sub>3</sub>, VSbO<sub>4</sub>, Ag<sub>3</sub>RuO<sub>4</sub>, TiCu<sub>3</sub>O<sub>4</sub>, and TlCuO<sub>2</sub>. The other 71 candidates, although non-conducting, can potentially be considered as anodes in photocatalytic mechanisms for OER. The discovery of a potential candidate for OER demonstrates the potential of ML-assisted screening techniques in identifying novel catalysts.

## 4 Conclusions

In this contribution, we employed pre-trained machine learning potentials from the Open Catalyst Project to develop a publicly available database of O\* and OH\* surface intermediates for 4,119 oxide materials. We demonstrated the utility and variability of this database by presenting several easily implemented high-throughput screening frameworks for identifying thermodynamically stable and catalytically active (low overpotential) materials for oxygen evolution reaction from our initial pool of 4,119 candidates. Our first screening framework identified 81 candidates that are Pourbaix stable in the bulk regime with catalytic surfaces that appear on the Wulff shape. By slightly modifying this framework to account for the possibility of nanoscale stability, we identified 121 additional candidates. Additional modifications to the reaction conditions and our definition of Pourbaix stability yields a total of 190 candidates with 27 unexplored candidates fulfilling additional criteria of being non-toxic and conductive. Furthermore, we were able to validate our predictions with DFT calculations from the literature as well as our own. When ignoring material cost and bulk stability, we find that oxides containing Cr, Mn, Co, Cu, Se, Sb, Bi, Pb, and

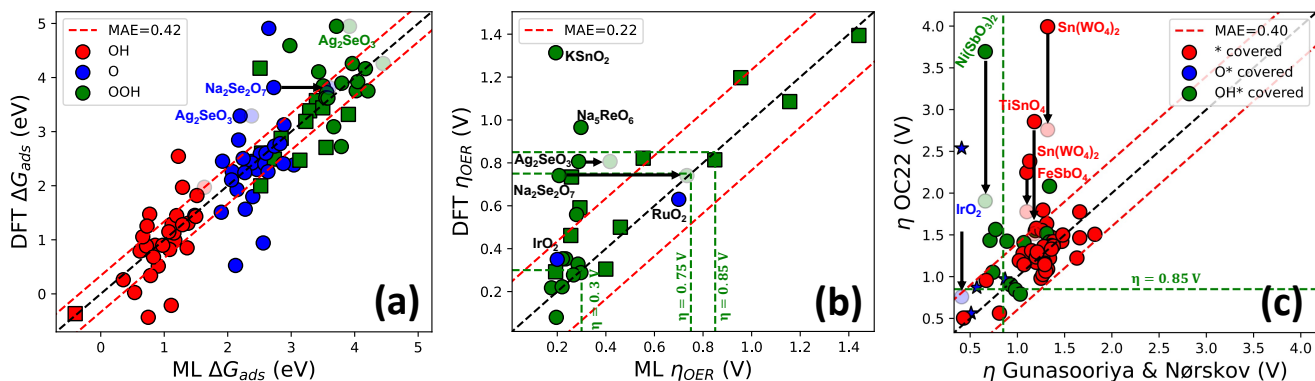


Figure 7: (a) DFT calculated data points for reaction energy plotted against the corresponding ML predicted quantities. (b) DFT calculated data points for overpotential plotted against the corresponding ML predicted quantities. Overpotentials of the benchmark materials are highlighted in blue ( $\text{IrO}_2$  and  $\text{RuO}_2$ ). Overpotentials of less than 0.75 eV are considered catalytically active. Square data points indicate desorption or dissociation of the intermediate. Transparent data points correspond to ML predicted data points with spring constraints applied to prevent desorption and dissociation events.

Tl tend to exhibit overpotentials that are possibly competitive with current benchmark materials ( $\text{IrO}_2$  and  $\text{RuO}_2$ ). We plan to further expand our database to include other potential reaction mechanisms for OER such as the oxocoupling mechanism and lattice oxygen evolution. We hope this database will encourage future investigators to develop their own high-throughput screening frameworks.

## Author Contributions

Richard Tran implemented the screening framework and performed DFT calculations. Liqiang Huang designed the parameters and software to manage and automate predictions and performed ML predictions. Yuan Zi, Shengguang Wang, and Benjamin M. Comer defined the overall goal of the project and provided scientific insight and solutions. Lars Grabow defined the DFT aspect of the work. Jiefu Chen and Xuqing Wu defined machine learning aspect of the work. Jiefu Chen and Lars Grabow acquired funding for the project. Ligang Lu initiated and funded the project and recruited Shell Subject Matter Experts to the project. Ligang Lu, Stefan J. Raaijman, Nishant K. Sinha, Sajanikumari Sadasivan, Shibin Thundiyil, Kuldeep B. Mamtani, and Ganesh Iyer defined the industrial benchmarks and

goals of the project. All authors contributed to and commented on the manuscript.

## Conflicts of interest

This project is supported by Shell US.

## Data Availability

Data for this article, including including the ML predicted initial and relaxed structures and total energies are available at the University of Houston Dataverse Repository at <https://doi.org/10.18738/T8/APJFTM>.<sup>57</sup> Details regarding the database metadata are given in the Supplementary Information. The code for all analysis and data generation can be found on Github with DOI: 10.5281/zenodo.12616291.

## Acknowledgements

The authors gratefully acknowledge financial support from Shell US. The authors also gratefully acknowledge financial support from the University of Houston Energy Transition Institute. This research was performed using computational resources from the Carya, Opuntia, and Sabine clusters provided by the Research Computing Data Core at the University of Houston.

## References

- (1) Jamesh, M. I.; Sun, X. Recent progress on earth abundant electrocatalysts for oxygen evolution reaction (OER) in alkaline medium to achieve efficient water splitting – A review. *Journal of Power Sources* **2018**, *400*, 31–68.
- (2) Yuan, N.; Jiang, Q.; Li, J.; Tang, J. A review on non-noble metal based electrocatalysis for the oxygen evolution reaction. *Arabian Journal of Chemistry* **2020**, *13*, 4294–4309.
- (3) Kim, J. S.; Kim, B.; Kim, H.; Kang, K. Recent Progress on Multimetal Oxide Catalysts for the Oxygen Evolution Reaction. *Advanced Energy Materials* **2018**, *8*, 1–26.
- (4) Suen, N. T.; Hung, S. F.; Quan, Q.; Zhang, N.; Xu, Y. J.; Chen, H. M. Electrocatalysis for the oxygen evolution reaction: Recent development and future perspectives. *Chemical Society Reviews* **2017**, *46*, 337–365.
- (5) Lee, Y.; Suntivich, J.; May, K. J.; Perry, E. E.; Shao-Horn, Y. Synthesis and activities of rutile IrO<sub>2</sub> and RuO<sub>2</sub> nanoparticles for oxygen evolution in acid and alkaline solutions. *Journal of Physical Chemistry Letters* **2012**, *3*, 399–404.
- (6) Free Metal Price Tables and Charts. <https://www.dailymetalprice.com/>.
- (7) Precious Metals Dealer. <https://www.apmex.com/>.
- (8) Latest and Historical Metal Prices. [www.metalarary.com](http://www.metalarary.com).
- (9) Wang, Z.; Zheng, Y. R.; Chorkendorff, I.; Nørskov, J. K. Acid-Stable Oxides for Oxygen Electrocatalysis. *ACS Energy Letters* **2020**, *5*, 2905–2908.
- (10) Gunasooriya, G. T. K.; Nørskov, J. K. Analysis of Acid-Stable and Active Oxides for the Oxygen Evolution Reaction. *ACS Energy Letters* **2020**, *5*, 3778–3787.
- (11) Abed, J.; Heras-Domingo, J.; Luo, M.; Sanspeur, R.; Alnoush, W.; Meira, D.; Wang, H.-T.; Wang, J.; Zhou, J.; Zhou, D., et al. Multi-Descriptor Design of Ruthenium Catalysts for Durable Acidic Water Oxidation. *Preprint* **2023**, 23.
- (12) Fu, J.; Jiang, X.; Han, W.; Cao, Z. Enhancing the Cycling Stability of Transition-Metal-Oxide-Based Electrochemical Electrode via Pourbaix Diagram Engineering. *Energy Storage Materials* **2021**, *42*, 252–258.
- (13) Kang, S.; Mo, Y.; Ong, S. P.; Ceder, G. Nanoscale stabilization of sodium oxides: Implications for Na-O<sub>2</sub> batteries. *Nano Letters* **2014**, *14*, 1016–1020.
- (14) Sun, W. Theoretical Advancements towards Understanding Crystalline Metastability during Materials Synthesis. Ph.D. thesis, Massachusetts Institute of Technology, 2016.
- (15) Navrotsky, A. Nanoscale effects on thermodynamics and phase equilibria in oxide systems. *ChemPhysChem* **2011**, *12*, 2207–2215.
- (16) Li, Z.; Achenie, L. E.; Xin, H. An Adaptive Machine Learning Strategy for Accelerating Discovery of Perovskite Electrocatalysts. *ACS Catalysis* **2020**, *10*, 4377–4384.
- (17) Rao, K. K.; Do, Q. K.; Pham, K.; Maiti, D.; Grabow, L. C. Extendable Machine Learning Model for the Stability of Single Atom Alloys. *Topics in Catalysis* **2020**, *63*, 728–741.
- (18) Abdelfatah, K.; Yang, W.; Vijay Solomon, R.; Rajbanshi, B.; Chowdhury, A.; Zare, M.; Kundu, S. K.;

- Yonge, A.; Heyden, A.; Terejanu, G. Prediction of Transition-State Energies of Hydrodeoxygenation Reactions on Transition-Metal Surfaces Based on Machine Learning. *Journal of Physical Chemistry C* **2019**, *123*, 29804–29810.
- (19) Malek, A.; Wang, Q.; Baumann, S.; Guillon, O.; Eikerling, M.; Malek, K. A Data-Driven Framework for the Accelerated Discovery of CO<sub>2</sub> Reduction Electrocatalysts. *Frontiers in Energy Research* **2021**, *9*, 1–15.
- (20) Back, S.; Yoon, J.; Tian, N.; Zhong, W.; Tran, K.; Ulissi, Z. W. Convolutional Neural Network of Atomic Surface Structures to Predict Binding Energies for High-Throughput Screening of Catalysts. *Journal of Physical Chemistry Letters* **2019**, *10*, 4401–4408.
- (21) Chanussot, L. et al. Open Catalyst 2020 (OC20) Dataset and Community Challenges. *ACS Catalysis* **2021**, *11*, 6059–6072.
- (22) Tran, R.; Wang, D.; Kingsbury, R.; Palizhati, A.; Persson, K. A.; Jain, A.; Ulissi, Z. W. Screening of bimetallic electrocatalysts for water purification with machine learning. *The Journal of Chemical Physics* **2022**, *157*, 074102.
- (23) Price, C. C.; Singh, A.; Frey, N. C.; Shenoy, V. B. Efficient catalyst screening using graph neural networks to predict strain effects on adsorption energy. *Science Advances* **2022**, *8*, 1–12.
- (24) Tran, R. et al. The Open Catalyst 2022 (OC22) Dataset and Challenges for Oxide Electrocatalysts. *ACS Catalysis* **2022**, *13*, 3066–3084.
- (25) Ong, S. P.; Richards, W. D.; Jain, A.; Hautier, G.; Kocher, M.; Cholia, S.; Gunter, D.; Chevrier, V. L.; Persson, K. A.; Ceder, G. Python Materials Genomics (pymatgen): A robust, open-source python library for materials analysis. *Computational Materials Science* **2013**, *68*, 314–319.
- (26) Persson, K. a.; Waldwick, B.; Lazic, P.; Ceder, G. Prediction of solid-aqueous equilibria: Scheme to combine first-principles calculations of solids with experimental aqueous states. *Physical Review B - Condensed Matter and Materials Physics* **2012**, *85*, 1–12.
- (27) Singh, A. K.; Zhou, L.; Shinde, A.; Suram, S. K.; Montoya, J. H.; Winston, D.; Gregoire, J. M.; Persson, K. A. Electrochemical Stability of Metastable Materials. *Chemistry of Materials* **2017**, *29*, 10159–10167.
- (28) Patel, A. M.; Nørskov, J. K.; Persson, K. A.; Montoya, J. H. Efficient Pourbaix diagrams of many-element compounds. *Physical Chemistry Chemical Physics* **2019**, *21*, 25323–25327.
- (29) Hjorth Larsen, A. et al. The atomic simulation environment - A Python library for working with atoms. *Journal of Physics Condensed Matter* **2017**, *29*, 1–30.
- (30) Jain, A.; Ong, S. P.; Hautier, G.; Chen, W.; Richards, W. D.; Dacek, S.; Cholia, S.; Gunter, D.; Skinner, D.; Ceder, G.; Persson, K. A. Commentary: The materials project: A materials genome approach to accelerating materials innovation. *APL Materials* **2013**, *1*, 011002 1.
- (31) Sun, W.; Ceder, G. Efficient creation and convergence of surface slabs. *Surface Science* **2013**, *617*, 53–59.
- (32) Montoya, J. H.; Persson, K. A. A high-throughput framework for determining adsorption energies on solid surfaces. *npj Computational Materials* **2017**, *3*, 14.



- (33) Kresse, G.; Hafner, J. Ab initio molecular dynamics for liquid metals. *Physical Review B* **1993**, *47*, 558–561.
- (34) Kresse, G.; Hafner, J. Ab initio molecular-dynamics simulation of the liquid-metalamorphous- semiconductor transition in germanium. *Physical Review B* **1994**, *49*, 14251–14269.
- (35) Kresse, G.; Furthmüller, J. Efficient iterative schemes for ab initio total-energy calculations using a plane-wave basis set. *Physical review. B, Condensed matter* **1996**, *54*, 11169–11186.
- (36) Kresse, G., Furthmuller, J. Software VASP, Vienna. *Physical Review B* **1996**, *54*, 169.
- (37) Blöchl, P. E. Projector augmented-wave method. 1994.
- (38) Perdew, J.; Burke, K.; Ernzerhof, M. Generalized Gradient Approximation Made Simple. *Physical review letters* **1996**, *77*, 3865–3868.
- (39) Jain, A.; Hautier, G.; Ong, S. P.; Moore, C. J.; Fischer, C. C.; Persson, K. A.; Ceder, G. Formation enthalpies by mixing GGA and GGA+U calculations. *Physical Review B* **2011**, *84*, 045115.
- (40) Gasteiger, J.; Sriram, A.; Günnemann, S.; Ulissi, Z. GemNet-OC : Developing Graph Neural Networks for Large and Diverse Molecular Simulation Datasets. *Transactions on Machine Learning Research* **2022**, 1–22.
- (41) Peterson, A. A. Global optimization of adsorbate-surface structures while preserving molecular identity. *Topics in Catalysis* **2014**, *57*, 40–53.
- (42) Musielewicz, J.; Wang, X.; Tian, T.; Ulissi, Z. FINETUNA: fine-tuning accelerated molecular simulations. *Machine Learning: Science and Technology* **2022**, *3*, 03LT01.
- (43) Wang, A.; Kingsbury, R.; McDermott, M.; Horton, M.; Jain, A.; Ong, S. P.; Dwaraknath, S.; Persson, K. A. A framework for quantifying uncertainty in DFT energy corrections. *Scientific Reports* **2021**, *11*, 1–10.
- (44) Shi, G.; Tano, T.; Tryk, D. A.; Yamaguchi, M.; Iiyama, A.; Uchida, M.; Iida, K.; Arata, C.; Watanabe, S.; Kakimoto, K. Temperature Dependence of Oxygen Evolution Reaction Activity in Alkaline Solution at Ni-Co Oxide Catalysts with Amorphous/Crystalline Surfaces. *ACS Catalysis* **2022**, *12*, 14209–14219.
- (45) Man, I. C.; Su, H.-Y.; Calle-Vallejo, F.; Hansen, H. A.; Martínez, J. I.; Inoglu, N. G.; Kitchin, J.; Jaramillo, T. F.; Nørskov, J. K.; Rossmeisl, J. Universality in Oxygen Evolution Electrocatalysis on Oxide Surfaces. *ChemCatChem* **2011**, *3*, 1159–1165.
- (46) Fabbri, E.; Haberer, A.; Waltar, K.; Kötz, R.; Schmidt, T. J. Developments and perspectives of oxide-based catalysts for the oxygen evolution reaction. *Catalysis Science and Technology* **2014**, *4*, 3800–3821.
- (47) Reier, T.; Nong, H. N.; Teschner, D.; Schlögl, R.; Strasser, P. Electrocatalytic Oxygen Evolution Reaction in Acidic Environments – Reaction Mechanisms and Catalysts. *Advanced Energy Materials* **2017**, *7*, 1–18.
- (48) Dau, H.; Limberg, C.; Reier, T.; Risch, M.; Roggan, S.; Strasser, P. The Mechanism of Water Oxidation: From Electrolysis via Homogeneous to Biological Catalysis. *ChemCatChem* **2010**, *2*, 724–761.
- (49) Fabbri, E.; Schmidt, T. J. Oxygen Evolution Reaction - The Enigma in Water Electrolysis. *ACS Catalysis* **2018**, *8*, 9765–9774.

- (50) González, D.; Heras-Domingo, J.; Sodupe, M.; Rodríguez-Santiago, L.; Solans-Monfort, X. Importance of the oxyl character on the IrO<sub>2</sub> surface dependent catalytic activity for the oxygen evolution reaction. *Journal of Catalysis* **2021**, *396*, 192–201.
- (51) Zhang, J.; Tao, H. B.; Kuang, M.; Yang, H. B.; Cai, W.; Yan, Q.; Mao, Q.; Liu, B. Advances in Thermodynamic-Kinetic Model for Analyzing the Oxygen Evolution Reaction. *ACS Catalysis* **2020**, *10*, 8597–8610.
- (52) Fornaciari, J. C.; Weng, L. C.; Alia, S. M.; Zhan, C.; Pham, T. A.; Bell, A. T.; Ogitsu, T.; Danilovic, N.; Weber, A. Z. Mechanistic understanding of pH effects on the oxygen evolution reaction. *Electrochimica Acta* **2022**, *405*, 1–8.
- (53) Huang, J.; Li, M.; Eslamibidgoli, M. J.; Eikerling, M.; Groß, A. Cation Overcrowding Effect on the Oxygen Evolution Reaction. *JACS Au* **2021**, *1*, 1752–1765.
- (54) Nishimoto, T.; Shinagawa, T.; Naito, T.; Takanabe, K. Microkinetic assessment of electrocatalytic oxygen evolution reaction over iridium oxide in unbuffered conditions. *Journal of Catalysis* **2020**, *391*, 435–445.
- (55) Mefford, J. T.; Zhao, Z.; Bajdich, M.; Chueh, W. C. Interpreting Tafel behavior of consecutive electrochemical reactions through combined thermodynamic and steady state microkinetic approaches. *Energy and Environmental Science* **2020**, *13*, 622–634.
- (56) Naito, T.; Shinagawa, T.; Nishimoto, T.; Takanabe, K. Recent advances in understanding oxygen evolution reaction mechanisms over iridium oxide. *Inorganic Chemistry Frontiers* **2021**, *8*, 2900–2917.
- (57) Tran, R. Replication Data for: Rational design of oxide catalysts for OER with OC22. 2023; <https://doi.org/10.18738/T8/APJFTM>.
- (58) Jain, A.; Wang, Z.; Nørskov, J. K. Stable Two-Dimensional Materials for Oxygen Reduction and Oxygen Evolution Reactions. *ACS Energy Letters* **2019**, *4*, 1410–1411.
- (59) Sanspeur, R. Y.; Heras-Domingo, J.; Kitchin, J. R.; Ulissi, Z. WhereWulff: A Semiautonomous Workflow for Systematic Catalyst Surface Reactivity under Reaction Conditions. *Journal of Chemical Information and Modeling* **2023**, *63*, 2427–2437.
- (60) Aykol, M.; Dwaraknath, S. S.; Sun, W.; Persson, K. A. Thermodynamic limit for synthesis of metastable inorganic materials. *Science Advances* **2018**, *4*, 1–8.
- (61) Joya, K. S.; Ahmad, Z.; Joya, Y. F.; Garcia-Esparza, A. T.; De Groot, H. J. Efficient electrochemical water oxidation in neutral and near-neutral systems with a nanoscale silver-oxide catalyst. *Nanoscale* **2016**, *8*, 15033–15040.
- (62) Simondson, D.; Chatti, M.; Gardiner, J. L.; Kerr, B. V.; Hoogeveen, D. A.; Cherepanov, P. V.; Kuschnerus, I. C.; Nguyen, T. D.; Johannessen, B.; Chang, S. L.; Macfarlane, D. R.; Hocking, R. K.; Simonov, A. N. Mixed Silver-Bismuth Oxides: A Robust Oxygen Evolution Catalyst Operating at Low pH and Elevated Temperatures. *ACS Catalysis* **2022**, *12*, 12912–12926.
- (63) Huang, X.; Xie, M.; Chen, Y.; Zong, Q.; Liu, Z.; Jin, Y. Copper-silver oxide nanowires grown on an alloy electrode as an efficient electrocatalyst for water oxidation. *RSC Advances* **2015**, *5*, 26150–26156.
- (64) Yu, M.; hee Moon, G.; Castillo, R. G.; DeBeer, S.; Weidenthaler, C.;

- Tüysüz, H. Dual Role of Silver Moieties Coupled with Ordered Mesoporous Cobalt Oxide towards Electrocatalytic Oxygen Evolution Reaction. *Angewandte Chemie - International Edition* **2020**, *59*, 16544–16552.
- (65) Zhao, X.; Zhang, H.; Yan, Y.; Cao, J.; Li, X.; Zhou, S.; Peng, Z.; Zeng, J. Engineering the Electrical Conductivity of Lamellar Silver-Doped Cobalt(II) Selenide Nanobelts for Enhanced Oxygen Evolution. *Angewandte Chemie - International Edition* **2017**, *56*, 328–332.
- (66) Tian, L.; Zhai, X.; Wang, X.; Li, J.; Li, Z. Advances in manganese-based oxides for oxygen evolution reaction. *Journal of Materials Chemistry A* **2020**, *8*, 14400–14414.
- (67) Teng, Y.; Wang, X. D.; Liao, J. F.; Li, W. G.; Chen, H. Y.; Dong, Y. J.; Kuang, D. B. Atomically Thin Defect-Rich Fe–Mn–O Hybrid Nanosheets as High Efficient Electrocatalyst for Water Oxidation. *Advanced Functional Materials* **2018**, *28*, 1–8.
- (68) Hong, J. S.; Seo, H.; Lee, Y. H.; Cho, K. H.; Ko, C.; Park, S.; Nam, K. T. Nickel-Doping Effect on Mn<sub>3</sub>O<sub>4</sub> Nanoparticles for Electrochemical Water Oxidation under Neutral Condition. *Small Methods* **2020**, *4*, 1–7.
- (69) Hu, C.; Zhang, L.; Zhao, Z. J.; Li, A.; Chang, X.; Gong, J. Synergism of Geometric Construction and Electronic Regulation: 3D Se-(NiCo)<sub>Sx</sub>/(OH)<sub>x</sub> Nanosheets for Highly Efficient Overall Water Splitting. *Advanced Materials* **2018**, *30*, 1–8.
- (70) Zhou, L.; Wang, Y.; Kan, K.; Lucana, D. M.; Guevarra, D.; Lai, Y.; Gregoire, J. M. Surveying Metal Antimonate Photoanodes for Solar Fuel Generation. *ACS Sustainable Chemistry and Engineering* **2022**, *10*, 15898–15908.
- (71) Zhou, L.; Li, H.; Lai, Y.; Richter, M.; Kan, K.; Haber, J. A.; Kelly, S.; Wang, Z.; Lu, Y.; Kim, R. S.; Li, X.; Yano, J.; Nørskov, J. K.; Gregoire, J. M. Stability and Activity of Cobalt Antimonate for Oxygen Reduction in Strong Acid. *ACS Energy Letters* **2022**, *7*, 993–1000.
- (72) Luke, S.; Chatti, M.; Yadav, A.; Kerr, B. V.; Kangsabanik, J.; Williams, T.; Cherepanov, P. V.; Johannessen, B.; Tanksale, A.; MacFarlane, D. R.; Hocking, R. K.; Alam, A.; Yella, A.; Simonov, A. N. Mixed metal-antimony oxide nanocomposites: low pH water oxidation electrocatalysts with outstanding durability at ambient and elevated temperatures. *Journal of Materials Chemistry A* **2021**, *9*, 27468–27484.
- (73) Gupta, S.; Fernandes, R.; Patel, R.; Spreitzer, M.; Patel, N. A review of cobalt-based catalysts for sustainable energy and environmental applications. *Applied Catalysis A: General* **2023**, *661*, 23.
- (74) Si, C.; Zhang, Y.; Zhang, C.; Gao, H.; Ma, W.; Lv, L.; Zhang, Z. Mesoporous nanostructured spinel-type MFe<sub>2</sub>O<sub>4</sub> (M = Co, Mn, Ni) oxides as efficient bi-functional electrocatalysts towards oxygen reduction and oxygen evolution. *Electrochimica Acta* **2017**, *245*, 829–838.
- (75) Li, M.; Xiong, Y.; Liu, X.; Bo, X.; Zhang, Y.; Han, C.; Guo, L. Facile synthesis of electrospun MFe<sub>2</sub>O<sub>4</sub> (M = Co, Ni, Cu, Mn) spinel nanofibers with excellent electrocatalytic properties for oxygen evolution and hydrogen peroxide reduction. *Nanoscale* **2015**, *7*, 8920–8930.
- (76) Müllner, M.; Riva, M.; Kraushofer, F.; Schmid, M.; Parkinson, G. S.; Mertens, S. F.; Diebold, U. Stability and Catalytic Performance of Reconstructed Fe<sub>3</sub>O<sub>4</sub> (001) and Fe

- 3 O 4 (110) Surfaces during Oxygen Evolution Reaction. *Journal of Physical Chemistry C* **2019**, *123*, 8304–8311.
- (77) Hirai, S.; Yagi, S.; Seno, A.; Fujioka, M.; Ohno, T.; Matsuda, T. Enhancement of the oxygen evolution reaction in Mn<sup>3+</sup>-based electrocatalysts: Correlation between Jahn-Teller distortion and catalytic activity. *RSC Advances* **2016**, *6*, 2019–2023.
- (78) Al-Mamun, M.; Su, X.; Zhang, H.; Yin, H.; Liu, P.; Yang, H.; Wang, D.; Tang, Z.; Wang, Y.; Zhao, H. Strongly Coupled CoCr<sub>2</sub>O<sub>4</sub>/Carbon Nanosheets as High Performance Electrocatalysts for Oxygen Evolution Reaction. *Small* **2016**, *12*, 2866–2871.
- (79) Quan, Z.; Wang, Y.; Fang, J. High-index faceted noble metal nanocrystals. *Accounts of Chemical Research* **2013**, *46*, 191–202.
- (80) Wang, Z.; Guo, X.; Montoya, J.; Nørskov, J. K. Predicting aqueous stability of solid with computed Pourbaix diagram using SCAN functional. *npj Computational Materials* **2020**, *6*, 1–7.
- (81) Konno, Y.; Yamamoto, T.; Nagayama, T. Nanoporous manganese ferrite films by anodising electroplated Fe-Mn alloys for bifunctional oxygen electrodes. *Nanoscale* **2021**, *13*, 12738–12749.
- (82) Han, J.; Zhang, M.; Bai, X.; Duan, Z.; Tang, T.; Guan, J. Mesoporous Mn-Fe oxyhydroxides for oxygen evolution. *Inorganic Chemistry Frontiers* **2022**, 3559–3565.
- (83) Sun, L.; Dai, Z.; Zhong, L.; Zhao, Y.; Cheng, Y.; Chong, S.; Chen, G.; Yan, C.; Zhang, X.; Tan, H.; Zhang, L.; Dinh, K. N.; Li, S.; Ma, F.; Yan, Q. Lattice strain and atomic replacement of CoO<sub>6</sub> octahedra in layered sodium cobalt oxide for boosted water oxidation electrocatalysis. *Applied Catalysis B: Environmental* **2021**, *297*, 120477.
- (84) Toxic Metals - Overview. <https://www.osha.gov/toxic-metals>.
- (85) Yu, X.; Qu, L.; Lee, C.; Peng, J.; Yan, Q.; Bai, H.; Yao, M. Bismuth-nickel bimetal nanosheets with a porous structure for efficient hydrogen production in neutral and alkaline media. *Nanoscale* **2022**, *5*.
- (86) Kuznetsov, D. A.; Peng, J.; Giordano, L.; Román-Leshkov, Y.; Shao-Horn, Y. Bismuth Substituted Strontium Cobalt Perovskites for Catalyzing Oxygen Evolution. *Journal of Physical Chemistry C* **2020**, *124*, 6562–6570.
- (87) Thorarinsdottir, A. E.; Costentin, C.; Veroneau, S. S.; Nocera, D. G. P-Block Metal Oxide Noninnocence in the Oxygen Evolution Reaction in Acid: The Case of Bismuth Oxide. *Chemistry of Materials* **2022**, *34*, 826–835.
- (88) Bibi, I.; Alrowaily, A. W.; Alyousef, H. A.; Alotaibi, B. M.; Alqurashi, H.; Dahshan, A. Reduced graphene oxide-based silver selenide nanocomposite synthesized through hydrothermal method for oxygen evolution reaction. *Journal of Alloys and Compounds* **2024**, *993*, 174626.
- (89) Jiang, S.; Suo, H.; Zheng, X.; Zhang, T.; Lei, Y.; Wang, Y. X.; Lai, W. H.; Wang, G. Lightest Metal Leads to Big Change: Lithium-Mediated Metal Oxides for Oxygen Evolution Reaction. *Advanced Energy Materials* **2022**, *12*.
- (90) Zan, L.; Amin, H. M.; Mostafa, E.; Abd-El-Latif, A. A.; Iqbal, S.; Baltruschat, H. Electrodeposited Cobalt Nanosheets on Smooth Silver as a Bifunctional Catalyst for OER and ORR: In Situ Structural and Catalytic Characterization. *ACS Applied Materials and Interfaces* **2022**, *14*, 55458–55470.

- (91) Arslan Hamat, B.; Aydinol, M. K. Experimental investigation on the electrocatalytic behavior of Ag-based oxides, Ag<sub>2</sub>XO<sub>4</sub> (X= Cr, Mo, W), for the oxygen reduction reaction in alkaline media. *Journal of Solid State Chemistry* **2020**, *290*.
- (92) Singh, R. N.; Koenig, J. F.; Poillerat, G.; Chartier, P. Electrochemical Studies on Protective Thin Co<sub>3</sub>O<sub>4</sub> and NiCo<sub>2</sub>O<sub>4</sub> Films Prepared on Titanium by Spray Pyrolysis for Oxygen Evolution. *Journal of The Electrochemical Society* **1990**, *137*, 1408–1413.
- (93) Ahmed, J.; Alhokbany, N.; Ahamad, T.; Alshehri, S. M. Investigation of enhanced electro-catalytic HER/OER performances of copper tungsten oxide@reduced graphene oxide nanocomposites in alkaline and acidic media. *New J. Chem.* **2022**, *46*, 1267–1272.
- (94) Arora, A.; Wadhwa, R.; Yadav, K. K.; Ankush, J.; Jha, M. Enhanced electrochemical oxygen generation from silenite phase of bismuth iron oxide (Bi<sub>24</sub>Fe<sub>2</sub>O<sub>39</sub>) ultrafine particles stabilised at room temperature. *Journal of Electroanalytical Chemistry* **2024**, *958*, 118154.
- (95) Menezes, P. W.; Indra, A.; Bergmann, A.; Chernev, P.; Walter, C.; Dau, H.; Strasser, P.; Driess, M. Uncovering the prominent role of metal ions in octahedral: Versus tetrahedral sites of cobalt-zinc oxide catalysts for efficient oxidation of water. *Journal of Materials Chemistry A* **2016**, *4*, 10014–10022.
- (96) Kim, T. W.; Woo, M. A.; Regis, M.; Choi, K. S. Electrochemical synthesis of spinel type ZnCo<sub>2</sub>O<sub>4</sub> electrodes for use as oxygen evolution reaction catalysts. *Journal of Physical Chemistry Letters* **2014**, *5*, 2370–2374.
- (97) Du, C.; Yang, J.; Yang, J.; Zhao, Y.; Chen, R.; Shan, B. An iron oxide-copper bismuth oxide photoelectrochemical cell for spontaneous water splitting. *International Journal of Hydrogen Energy* **2018**, *43*, 22807–22814.
- (98) Balaghi, S. E.; Triana, C. A.; Patzke, G. R. Molybdenum-Doped Manganese Oxide as a Highly Efficient and Economical Water Oxidation Catalyst. *ACS Catalysis* **2020**, *10*, 2074–2087.
- (99) Hausmann, J. N.; Ashton, M.; Mebs, S.; Walter, C.; Selve, S.; Haumann, M.; Sontheimer, T.; Dau, H.; Driess, M.; Menezes, P. W. Intermetallic Cobalt-Indium Nanoparticles as Oxygen Evolution Reaction Precatalyst: A Non-Leaching p-Block Element. *Small* **2024**, *2309749*, 1–7.
- (100) Lima, A. J.; Silva, V. D.; Raimundo, R. A.; Morales, M. A.; Simões, T. A.; Loureiro, F. J.; Fagg, D. P.; Macedo, D. A.; Nascimento, R. M. Fe-doped calcium cobaltites as electrocatalysts for oxygen evolution reaction. *Ceramics International* **2021**, *47*, 26109–26118.
- (101) Bagheri, S.; Ramimoghdam, D.; Yousefi, A. T.; Hamid, S. B. A. Synthesis, characterization and electrocatalytic activity of silver doped-titanium dioxide nanoparticles. *International Journal of Electrochemical Science* **2015**, *10*, 3088–3097.
- (102) Simondson, D.; Chatti, M.; Bonke, S. A.; Tesch, M. F.; Golnak, R.; Xiao, J.; Hoogeveen, D. A.; Cherepanov, P. V.; Gardiner, J. L.; Tricoli, A.; MacFarlane, D. R.; Simonov, A. N. Stable Acidic Water Oxidation with a Cobalt-Iron-Lead Oxide Catalyst Operating via a Cobalt-Selective Self-Healing Mechanism. *Angewandte Chemie - International Edition* **2021**, *60*, 15821–15826.

- (103) Li, Y.; Zhang, X.; Zheng, Z. A Review of Transition Metal Oxygen-Evolving Catalysts Decorated by Cerium-Based Materials: Current Status and Future Prospects. *CCS Chemistry* **2022**, *4*, 31–53.
- (104) Tabassum, L.; Tasnim, H.; Shubhashish, S.; Perera, I.; Bhosale, T.; Li, M.; March, S.; Islam, M. K.; Suib, S. L. Selenium-doped copper oxide nanoarrays: Robust electrocatalyst for the oxygen evolution reaction with ultralow overpotential. *Applied Materials Today* **2022**, *27*, 101485.
- (105) Xu, Z.; Li, W.; Wang, X.; Wang, B.; Shi, Z.; Dong, C.; Yan, S.; Zou, Z. Novel Cobalt Germanium Hydroxide for Electrochemical Water Oxidation. *ACS Applied Materials and Interfaces* **2018**, *10*, 30357–30366.
- (106) Rajput, A.; Kundu, A.; Chakraborty, B. Recent Progress on Copper-Based Electrode Materials for Overall Water-Splitting. *ChemElectroChem* **2021**, *8*, 1698–1722.
- (107) Yu, M.; Budiyanoto, E.; Tüysüz, H. Principles of Water Electrolysis and Recent Progress in Cobalt-, Nickel-, and Iron-Based Oxides for the Oxygen Evolution Reaction. *Angewandte Chemie - International Edition* **2022**, *61*.
- (108) Cui, B.; Lin, H.; Li, J. B.; Li, X.; Yang, J.; Tao, J. Core-ring structured NiCo<sub>2</sub>O<sub>4</sub> nanoplatelets: Synthesis, characterization, and electrocatalytic applications. *Advanced Functional Materials* **2008**, *18*, 1440–1447.
- (109) Lin, X.; Bao, H.; Zheng, D.; Zhou, J.; Xiao, G.; Guan, C.; Zhang, L.; Wang, J. Q. An Efficient Family of Misfit-Layered Calcium Cobalt Oxide Catalyst for Oxygen Evolution Reaction. *Advanced Materials Interfaces* **2018**, *5*, 1–7.
- (110) Yue, Y.; Niu, J.; Yang, C.; Qin, J.; Zhang, X.; Liu, R. The OER/ORR activities of copper oxyhydroxide series electrocatalysts. *Molecular Catalysis* **2023**, *537*, 112942.
- (111) Wang, L.; Ge, X.; Li, Y.; Liu, J.; Huang, L.; Feng, L.; Wang, Y. Nickel enhanced the catalytic activities of amorphous copper for the oxygen evolution reaction. *Journal of Materials Chemistry A* **2017**, *5*, 4331–4334.
- (112) Zhang, Q.; Liu, N.; Guan, J. Charge-Transfer Effects in Fe-Co and Fe-Co-Y Oxides for Electrocatalytic Water Oxidation Reaction. *ACS Applied Energy Materials* **2019**, *2*, 8903–8911.
- (113) Huang, L.; Chen, D.; Luo, G.; Lu, Y. R.; Chen, C.; Zou, Y.; Dong, C. L.; Li, Y.; Wang, S. Zirconium-Regulation-Induced Bifunctionality in 3D Cobalt–Iron Oxide Nanosheets for Overall Water Splitting. *Advanced Materials* **2019**, *31*, 1–10.
- (114) Zhou, Z.; Li, X.; Li, Q.; Zhao, Y.; Pang, H. Copper-based materials as highly active electrocatalysts for the oxygen evolution reaction. *Materials Today Chemistry* **2019**, *11*, 169–196.
- (115) Frydendal, R.; Paoli, E. A.; Chorkendorff, I.; Rossmeisl, J.; Stephens, I. E. Toward an Active and Stable Catalyst for Oxygen Evolution in Acidic Media: Ti-Stabilized MnO<sub>2</sub>. *Advanced Energy Materials* **2015**, *5*.
- (116) Babu, S. P.; Falch, A. Recent Developments on Cr-Based Electrocatalysts for the Oxygen Evolution Reaction in Alkaline Media. *ChemCatChem* **2022**, *14*, e202200364.
- (117) Chen, X.; Wang, H.; Meng, R.; Xia, B.; Ma, Z. Cadmium Hydroxide: A Missing Non-Noble Metal Hydroxide Electrocatalyst for the Oxygen Evolution Reaction. *ACS Applied Energy Materials* **2020**, *3*, 1305–1310.

- (118) Song, X.; Yang, T.; Du, H.; Dong, W.; Liang, Z. New binary Mn and Cr mixed oxide electrocatalysts for the oxygen evolution reaction. *Journal of Electroanalytical Chemistry* **2016**, *760*, 59–63.
- (119) Han, X.; Zhang, T.; Du, J.; Cheng, F.; Chen, J. Porous calcium-manganese oxide microspheres for electrocatalytic oxygen reduction with high activity. *Chemical Science* **2013**, *4*, 368–376.

## 5 Supplementary Information

### 5.1 Surface energy

To the surface energy of all bare slabs, we begin with the surface grand potential given by:

$$\gamma = \frac{E_{slab} - \sum_i n_i \mu_i}{2A} \quad (9)$$

where  $E_{slab}$  is the total energy of the bare slab,  $n_i$  is the number of atom  $i$  in the slab,  $\mu_i$  is the chemical potential of atom  $i$ ,  $A$  is the surface area and the factor of  $\frac{1}{2}$  accounts for the two surfaces in the slab. We can define the chemical potential of each element as:

$$\mu_{A_x B_y O_z} = E_{bulk}^{A_x B_y O_z} = x\mu_A + y\mu_B + z\mu_O \quad (10)$$

where  $E_{bulk}^{A_x B_y O_z}$  is the total energy per formula unit of the bulk crystal. As such, the surface energy for stoichiometric slabs can be rewritten as:

$$\gamma = \frac{E_{slab}^{A_{nx} B_{ny} O_{nz}} - nE_{bulk}^{A_x B_y O_z}}{2A} \quad (11)$$

where  $n$  is the number of bulk formula units in the slab.

We reiterate that we enumerated through all terminations per facet by modelling slabs with symmetrically equivalent terminations on each side. Inevitably, this will require the removal or addition of cations and oxygen which will lead to non-stoichiometric (relative to the bulk) slab models. In such cases, we need to compensate for the excess or deficient components by introducing variable chemical potentials per component. For any slab, there can be up to  $n - 1$  excess or deficient components relative to the bulk. As an example, the surface energy of a slab of  $A_{nx} B_{ny+k} O_{nz-j}$  constructed from a bulk crystal of  $A_x B_y O_z$  becomes:

$$\gamma = \frac{E_{slab}^{A_{nx} B_{ny+k} O_{nz-j}} - (nE_{bulk}^{A_x B_y O_z} + k\mu_B - j\frac{1}{2}\mu_{O_2})}{2A} \quad (12)$$

The chemical potential of oxygen ( $\mu_{O_2}$ ) can be referenced to the electrochemical decomposition of water to  $O_{2(g)}$ :



given by:

$$\mu_{O_2} = 4.92 + 2G_{H_2O} - 4(\mu_{H^+} + \mu_{e^-}) + \Delta G_{corr}^{O^*} \quad (14)$$

where

$$G = E + ZPE - TS^o \quad (15)$$

We can relate the proton-electron pair ( $H^+ + e^-$ ) to the activity of the proton and the standard hydrogen electrode (SHE) using the Nernst Equation:

$$\mu_{H^+} + \mu_{e^-} = \frac{1}{2}G_{H_2} - eU + k_B T \ln a_{H^+} \quad (16)$$

Here  $a_{H^+}$  is the activity of a proton with  $-pH \ln 10 = \ln a_{H^+}$  and  $eU$  is the change in electron energy under an applied potential. An excess or deficient oxygen component in the slab can be treated as an adsorbed or desorbed species and to account for this, we included a correction term,  $\Delta G_{corr}^{O^*}$ , to derive the Gibbs free energy of adsorption from the DFT electronic  $O^*$  adsorption



energy (see Tran et al.<sup>24</sup> and Gunasooriya and Nørskov<sup>10</sup> for details in regards to corrections made for the Gibbs free energy). Consequently,  $\mu_{\text{O}}$  can be rewritten as a function of  $pH$  and  $U$  as such:

$$\mu_{\text{O}_2} = 4.92 + 2\mu_{\text{H}_2\text{O}} - 4\left(\frac{1}{2}\mu_{\text{H}_2} - eU + k_B T \ln a_{\text{H}^+}\right) + \Delta G_{\text{corr}}^{\text{O}^*} \quad (17)$$

It is typical to reference the chemical potential of B ( $\mu_B$ ) with respect to the per atom energy of the ground state bulk crystal of pure component B (e.g.  $\mu_{\text{Fe}} = \Delta\mu_{\text{Fe}} + E_{\text{BCC,Fe}}^{\text{DFT}}$ ). However, this is predicated upon the assumption that  $\text{A}_x\text{Fe}_y\text{O}_z$  will immediately decompose into pure solid BCC Fe at the surface. However, multicomponent systems generally do not immediately decompose into individual solid components of each element. Herein, we assume that an excess or deficiency of components B or O at the surface will lead to slight surface passivation with a decomposition of  $\text{A}_x\text{B}_y\text{O}_z$  into a more stable multicomponent guided by the phase diagram, e.g.:



In such a case, it makes sense to reference  $\mu_B$  with respect to the energy of  $\text{B}_y\text{O}_z$ :

$$\mu_{\text{B}_y\text{O}_z} = E_{\text{bulk}}^{\text{B}_y\text{O}_z} = y\mu_B + z\mu_{\text{O}} \quad (19)$$

Here, the chemical potential of B increases (or decreases) with the component of B at the surface, leading to a slight passivation of  $\text{A}_x\text{B}_y\text{O}_z$  to  $\text{B}_y\text{O}_z$  at the surface. We can thereby rewrite  $\mu_B$  as a function of  $\mu_{\text{O}}$

$$\mu_B = \frac{E_{\text{bulk}}^{\text{B}_y\text{O}_z} - z\mu_{\text{O}}}{y} \quad (20)$$

which can be substituted into Equation 12 in order to define surface energy purely as a function of  $\mu_{\text{O}}$  and by extension  $U$  and  $pH$  in accordance with Equation 17.

## 5.2 Nanoparticle formation energy

The nanoparticle formation energy ( $G_f^{\text{N}P}$ ) is given by Equation 4 in the main manuscript. For a material in the bulk regime ( $r > 100$  nm), we can assume that the thermodynamic contributions of the surface are negligible when compared to the contribution from the bulk. However, as the particle size continues to decrease, the surface-area-to-volume ratio will increase, resulting the properties of the surface dictating the properties of the overall material. Unlike the bulk formation energy ( $E_V(pH, V, T)(\frac{4}{3}\pi r^3)$ ),  $G_f^{\text{N}P}$  accounts for this by incorporating the surface energy contributions into the overall formation energy.

Here,  $\frac{4}{3}\pi r^3$  is the volume of a nanoparticle at radius  $r$  and  $E_V$  is the Pourbaix formation energy at a given  $pH$ ,  $U$ , and  $T$  per unit cell volume ( $E_{\text{PBX}}/V$ ) where  $E_{\text{PBX}}$  can be derived from the following:<sup>26-28</sup>

$$E_{\text{PBX}} = E_0 + k_B T \ln(10)pH - n_{\text{O}}\mu_{\text{H}_2\text{O}}^{\text{O}} + (n_{\text{H}} - 2n_{\text{O}})pH + n_{e^-}(-n_{\text{H}} + 2n_{\text{O}} + eU) \quad (21)$$

where  $n$  are the number of species in the system respectively and  $E_0$  is the formation energy of the bulk with respect to  $\text{H}_{2(\text{g})}$  and  $\text{O}_{2(\text{g})}$ :

$$E_0 = E_f + k_B T \ln(10)pH - n_{\text{H}_2\text{O}}\mu_{\text{H}_2\text{O}}^{\text{O}} \quad (22)$$

The contribution of the surface energy is given by  $\bar{\gamma}(4\pi r^2)$  where  $4\pi r^2$  is the surface area of the nanoparticle at radius  $r$  and  $\bar{\gamma}$  is the surface energy of the nanoparticle. In this study, the equilibrium crystal structure, or Wulff shape, serves as an analogue to the nanoparticle. The

Wulff shape is derived through the Wulff construction whereby a set of Miller index ( $hkl$ ) planes perpendicular to a vector from an origin at a distance proportional to  $\gamma_{hkl}$  (see Equation 1 in the main manuscript) enclose a polyhedron. The surface energy of this polyhedron is defined by:

$$\bar{\gamma}(pH, U, T, \Delta\mu_M) = \frac{\sum_{hkl} \gamma_{hkl}(pH, U, T, \Delta\mu_M) A_{hkl}}{\sum_{hkl} A_{hkl}} = \sum_{hkl} \gamma_{hkl} f_{hkl}^A(pH, U, T, \Delta\mu_M) \quad (23)$$

where ( $hkl$ ) are the facets that appear on the Wulff shape and  $f_{hkl}^A$  is the fraction of area occupied by facet ( $hkl$ ) on the Wulff shape.

Incorporating the surface energy contributions of the nanoparticle can consequently lead to some materials above the Pourbaix hull becoming more thermodynamically stable than the ground state material depending on the nanoparticle size.

### 5.3 Overpotential

The overpotential has been demonstrated to be an excellent predictor of catalytic activity in electrocatalytic processes. The overpotential ( $\eta$ ) describes the excess amount of applied potential required to move forward in each reaction step shown in Figure 3 relative to an ideal catalyst. The summation of each reaction energy (energetic height of each reaction step or  $\Delta G_{rxn}$ ) is defined as the standard reduction potential in Equation 13. The ideal catalyst equally distributes the standard reduction potential along each step to minimize the required energy needed to move the reaction in the forward direction. This required energy is the equilibrium potential of OER and is given as:

$$\frac{G_{O_2} + 2G_{H_2} - 2G_{H_2O}}{4e} = 1.23V \quad (24)$$

As such, the theoretical overpotential for an electrocatalyst is given by:

$$\eta^{OER} = \max(\Delta G_{rxn}^1, \Delta G_{rxn}^2, \Delta G_{rxn}^3, \Delta G_{rxn}^4)/e - 1.23V \quad (25)$$

where  $\max(\Delta G_{rxn}^1, \Delta G_{rxn}^2, \Delta G_{rxn}^3, \Delta G_{rxn}^4)$  is the reaction energy of the potential determining step or  $\Delta G_{rxn}^{RDS}$ .

The energy of each reaction step is relative to the energy of a bare slab and two water molecules in a vacuum, all of which are initially assumed to be non-interacting. Guided by Equations i-iv (see Figure 3, we can determine the DFT electronic adsorption energy of steps i-iii with the following:

$$E_{ads}^{OH^*} = E^{OH^*} + \frac{1}{2}E_{H_2} - E_{slab} - \mu_{H_2O}^o \quad (26)$$

$$E_{ads}^{O^*} = E^{O^*} + E_{H_2} - E_{slab} - \mu_{H_2O}^o \quad (27)$$

$$E_{ads}^{OOH^*} = E^{OOH^*} + \frac{3}{2}E_{H_2} - E_{slab} - 2\mu_{H_2O}^o \quad (28)$$

where  $E^{X^*}$  is the total energy of the surface intermediate with adsorbate  $X$  and  $E_X$  is the reference energy of the adsorbate in a gas. By incorporating the vibrational frequency contributions of the adsorbate on the surface in  $E^{ads*}$ , i.e. the zero point energy and entropy, we can derive the corresponding Gibbs adsorption energies for steps i-iv:

$$\Delta G^i = G^{OH^*} + \mu_{H^+} + \mu_{e^-} - E_{slab} - G_{H_2O} \quad (29)$$

$$\Delta G^{ii} = G^{O^*} + 2(\mu_{H^+} + \mu_{e^-}) - E_{slab} - G_{H_2O} \quad (30)$$

$$\Delta G^{iii} = G^{OOH^*} + 3(\mu_{H^+} + \mu_{e^-}) - E_{slab} - 2G_{H_2O} \quad (31)$$

$$\Delta G^{iv} = 4.92V = G_{O_2} + 4(\mu_{H^+} + \mu_{e^-}) - 2G_{H_2O} \quad (32)$$

As previously mentioned, a constant correction term ( $\Delta G_{corr}$ ) can also be added to Equations 26-28 to obtain  $\Delta G$ :

$$\Delta G^i = E_{ads}^{OH^*} + \Delta G_{corr}^{OH^*} + \mu_{H^+} + \mu_{e^-} \quad (33)$$

$$\Delta G^{ii} = E^{O^*} + \Delta G_{corr}^{OH^*} + 2(\mu_{H^+} + \mu_{e^-}) \quad (34)$$

$$\Delta G^{iii} = E^{OOH^*} + \Delta G_{corr}^{OH^*} + 3(\mu_{H^+} + \mu_{e^-}) \quad (35)$$

where  $G_{corr}^{OH^*}$ ,  $G_{corr}^{O^*}$ , and  $G_{corr}^{OOH^*}$  were derived in the Supplementary Information of OC22.<sup>24</sup> Alternatively, if  $E^{OOH^*}$  is unavailable, well known scaling relationships between  $\Delta G^{iii}$  and  $\Delta G^i$  can be used instead (Figure S8):

$$\Delta G^{iii} = \Delta G^i + 3.26 \quad (36)$$

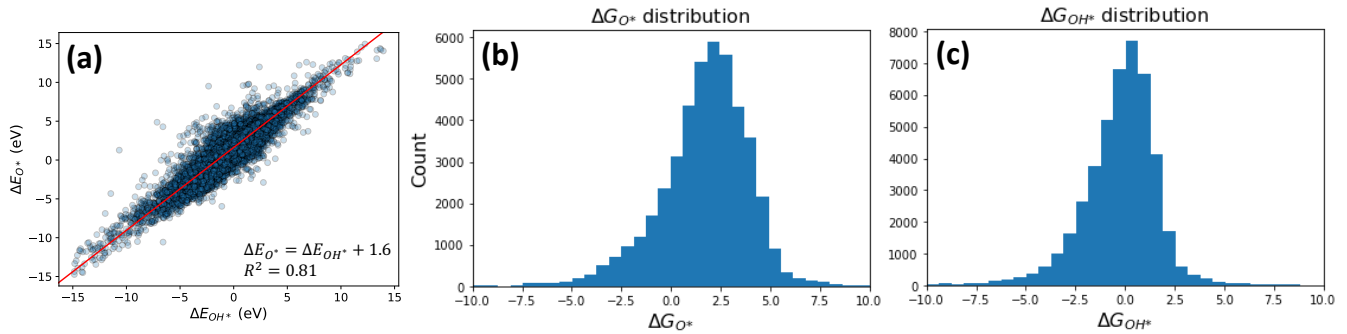


Figure 8: (a) Scaling relationship between  $\Delta G_{OH^*}$  and  $\Delta G_{O^*}$ . Binding energies of  $\Delta G > 15eV$  or  $\Delta G < -15eV$  were omitted from scaling relationship as anomalies. Distribution of adsorption energies for  $\Delta G_{O^*}$  (b) and  $\Delta G_{OH^*}$  (c).

From Equations 29-32 we can then obtain the individual reaction energies list in Figure 1:

$$\Delta G_{rxn}^1 = G^i \quad (37)$$

$$\Delta G_{rxn}^2 = G^{ii} - G^i \quad (38)$$

$$\Delta G_{rxn}^3 = G^{iii} - G^{ii} \quad (39)$$

$$\Delta G_{rxn}^4 = 4.92 - G^{iii} \quad (40)$$

## 5.4 Predictions of OOH\* and dissociation and desorption events

To save computational resources and time, we performed all initial assessments of  $\eta$  for all surfaces by predicting the Gibbs free energy of  $OH^*$  and  $O^*$  with ML and  $OOH^*$  using the scaling relationship provided by Equation 36. We acknowledge that this is a key intermediate in the WNA mechanism and by avoiding this step, it is unclear if candidate catalysts will undergo alternative mechanisms for OER. Furthermore, Equation 36 confines our exploration of overpotentials to the theoretical limit of 0.3-0.37 V regardless if any candidate studied can potentially break scaling relationships. Subsequently, we predicted the  $OOH^*$  intermediate for all surfaces exhibiting  $\eta < 0.75V$ . Figure S9(a) shows the  $OOH^*$  Gibbs free energy ( $\Delta G^{iii}$ ) of adsorption of these surfaces using Equation 36 (x-axis) and ML predicted  $E_{ads}^{OOH^*}$ . Although a large majority of data points lie within a MAE of 0.4 eV (62% or 5,861 out of 9,516 datapoints), we find that most data points beyond the MAE illustrates the predicted  $\Delta G^{iii}$  will severely underestimate the

corresponding value obtained through a scaling relationship. We also find that the majority of overpotential data points (65% or 2,324 out of 3,554 data points) assessed using both methods will consistently fall below 0.75 V, albeit with 2,368 within the MAE.

In predicting the overpotential of each surface, we also initially applied a spring constant of  $7.5\text{eV}/\text{\AA}^{-2}$  between all adsorbate atoms and  $2\text{eV}/\text{\AA}^{-2}$  between the surface and adsorbate to avoid desorption and dissociation events. However, this could lead to final geometries far away from the energy minima, resulting in poor energy predictions and unreliable geometries. Subsequently, for all predictions of intermediates that contributed to a free energy diagram exhibiting  $\eta < 0.75\text{V}$ , we performed additional ML relaxation steps on the final predicted geometries (obtained with constraints induced by the spring constant) *sans* the constraints. This two step relaxation process will help minimize the number of dissociation and desorption events when possible while providing the most reliable predicted geometries. Figure S9(c) plots the Gibbs free energy of the three intermediates obtained with constraints (x-axis) and without constraints (y-axis). We find the intermediates relaxing to a lower energy minima once the constraints were lifted. A large number of data points considered exhibit dissociation and/or desorption when the constraints were lifted resulting in a large MAE of 0.38 eV. A vast majority of these datapoints correspond to the  $\text{OOH}^*$  intermediate. However, the Gibbs free energy of adsorption for dissociated or desorbed intermediates can not be appropriately interpreted due to the lack of adsorption. As such, we also evaluated the MAE for intermediates where these events did not occur in both methods of predictions and demonstrated a more reasonable MAE of 0.17 eV. Figure S9(d) shows the corresponding overpotentials interpreted from these two sets of Gibbs free energy and shows a similar behavior in MAE when dissociation and desorption events are considered or omitted. Figure S9(e) shows a barplot distribution of the absolute difference in overpotential when considering the two methods of prediction. Although a significant amount of data points do exhibit dissociation and desorption with some overpotentials having inconsistent rate determining steps across the two methods, we see that these data points most correspond to larger disparities in overpotential with the majority of data points have a disparity of less than 0.25.

## 5.5 Database usage

The entire database including the initial and relaxed structures and total energies are freely available through the University of Houston Dataverse Repository.<sup>57</sup> The database comes in 4,119 .json files (one for each material assessed) with the mpid name followed by the '.json' suffix (e.g. mp-775737.json). Each file contains a list of dictionary objects. Each dictionary contains the metadata and predicted information of a specific surface and all the surface intermediates ( $\text{O}^*$ ,  $\text{OH}^*$ , and  $\text{OOH}^*$ ) of that surface and is structured as shown in Figure S10:

Metadata of each surface includes the Materials Project ID (entry\_id), the database from which the bulk structure used to generate the slab was obtained from (database), the chemical formula of the bulk (bulk\_reduced\_formula), a unique 20 character random ID that is assigned to all slabs considered (slab\_rid) with the 'slab-' prefix indicating a bare slab structure, the Miller index (miller\_index), the formula of the conventional unit cell (bulk\_formula), a *pymatgen* composition dictionary (bulk\_composition), the chemical system (bulk\_chemsys), the total energy of the DFT computed conventional bulk structure (bulk\_energy), the ML architecture used to perform the predictions (func), and a dictionary containing additional information pertaining to each individual adsorbed slab derived from the bare slab (slabs).

The keys of the slabs dictionary are the unique 20 character random ID corresponding to each slab (designated with the 'slab-' prefix) and adsorbed slab (designated with the 'adslab-' prefix). Each value of the dictionary represents a single prediction of a slab or adsorbed slab and contains its predicted properties and metadata properties. These properties are the lattice parameter matrix of the slab (cell), a list of atomic numbers making up the slab (atomic\_numbers), the

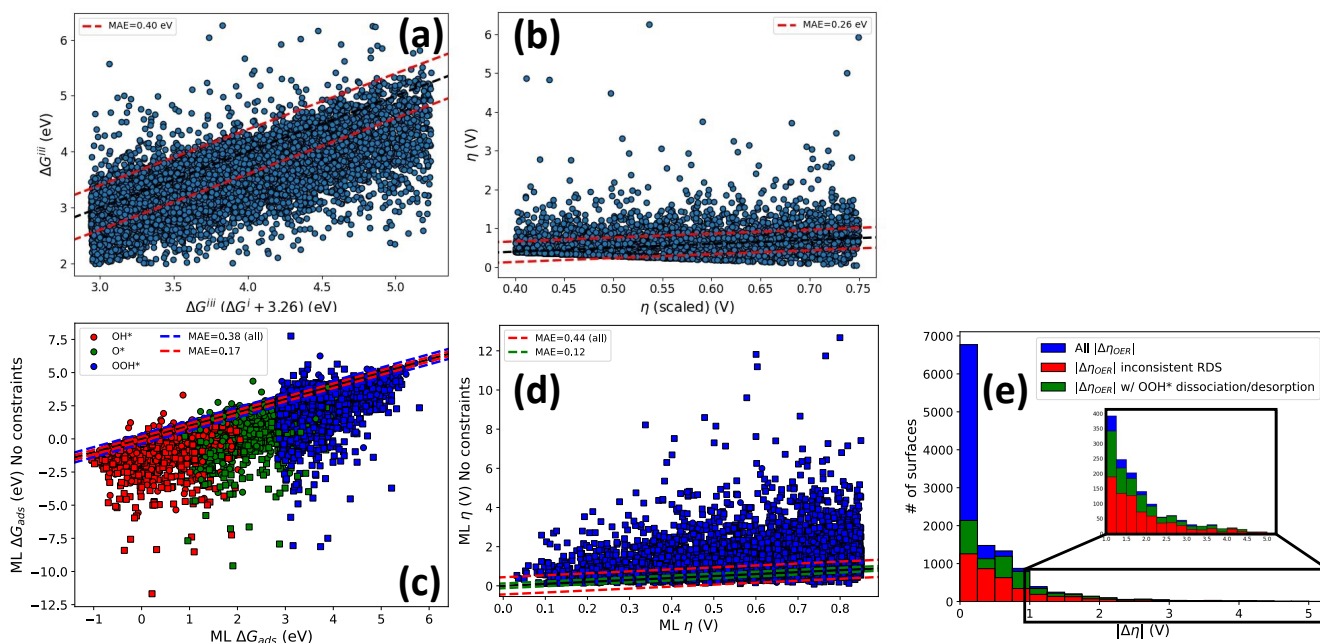


Figure 9: (a) Comparison of Gibbs free energy of adsorption for  $\text{OOH}^*$  ( $\Delta G^{iii}$ ) using Equation 36 (x-axis) vs  $\Delta G^{iii}$  using Equation 31 with ML predictions of  $E_{ads}^{\text{OOH}^*}$  (b) and the corresponding data points for overpotential. (c) Comparison of the Gibbs free energy of adsorption ( $\Delta G_{ads}$ ) with spring constraints to prevent adsorbate dissociation and desorption (x-axis) and without (y-axis) (d) and the corresponding data points for overpotential. Square data points indicate dissociation or desorption. The blue dashed line corresponds to an MAE when all data points are considered and the red dashed line indicates an MAE with dissociation and desorption events omitted. (e) Distribution in the absolute difference in overpotential between values calculated with and without the aforementioned constraints with an inset for datapoints exhibit a difference greater than 1.0 V.

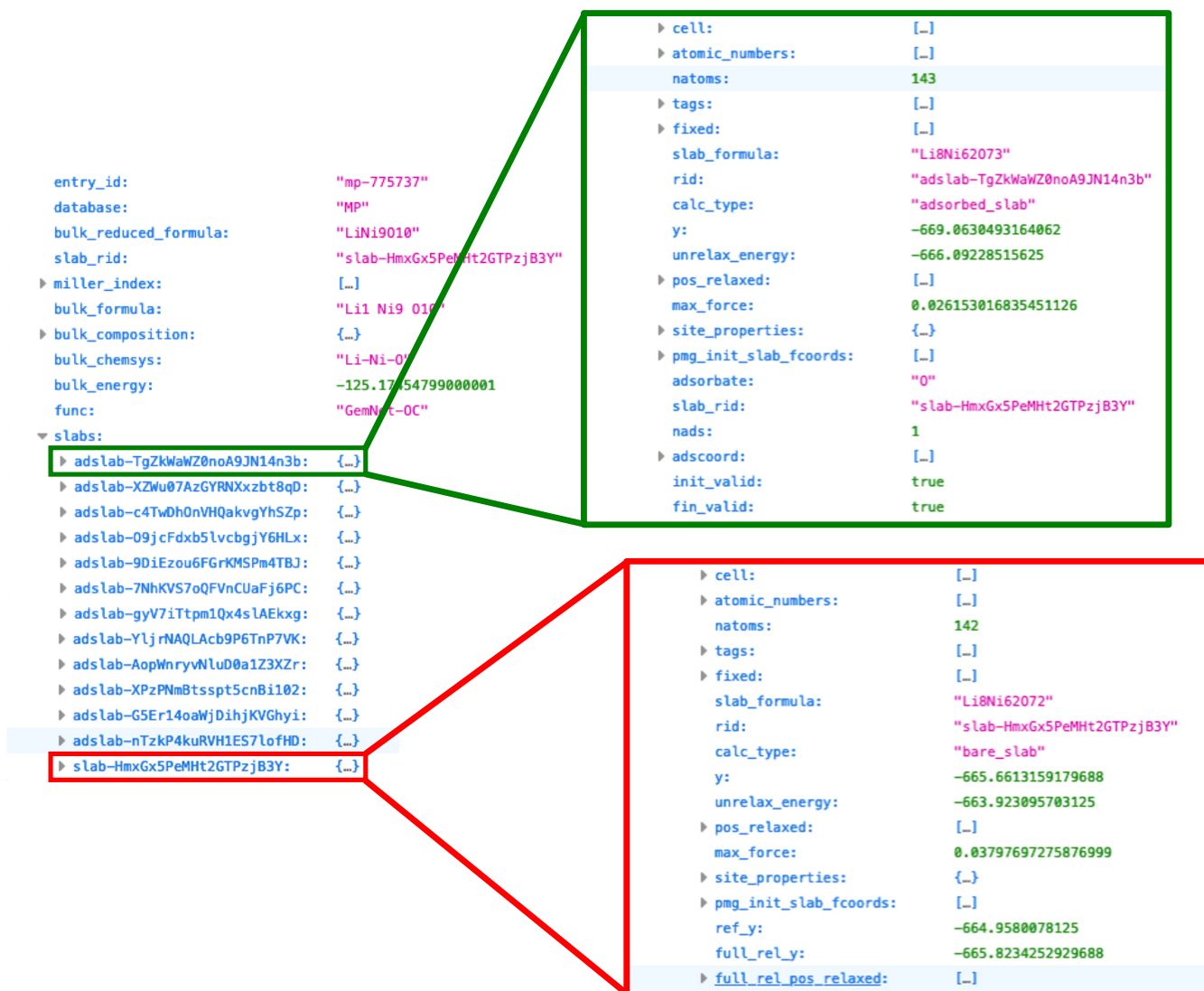


Figure 10: Dictionary object of a single entry in each database file.

number of atoms in the slab (natoms), tags indicating subsurface, surface and adsorbate atoms (tags), the index of atoms that were fixed during relaxation (fixed), the formula of the slab (slab\_formula), the random ID (rid), the type of calculation (calc\_type), the final energy (y), the unrelaxed energy (unrelax\_energy), the reference slab energy used for calculating adsorption energy (ref\_y) the relaxed xyz positions of all atoms in Cartesian coordinates (pos\_relaxed), the maximum force during the final relaxation step (max\_force), site properties such as the bulk Wyckoff positions (site\_properties), and the fractional crystal coordinates of the initial structure (pmg\_init\_slab\_fcoords). For entries corresponding to the adsorbed slabs, we also provided the random ID of the corresponding bare slab to help expedite binding energy calculations (slab\_rid), the fractional coordinate position of the adsorbate (slab\_rid) the intermediate (adsorbate), and the number of adsorbates (nads). As mentioned in the main manuscript, surfaces yielding low overpotentials of  $\eta_{OER} < 0.75V$  are also fully relaxed without the application of spring forces to maintain the intermediate identity and prevent desorption. These entries will have the relaxed energy (full\_rel\_y) and relaxed coordinates (full\_rel\_pos\_relaxed).

## 6 Candidate materials

Table 3: Summary of screening criteria for our final set of 190 candidate catalyst materials for OER across all screening frameworks with the formula, space group, number of facets on the Wulff shape with  $\eta < 0.75$  V, lowest overpotential across the facets, the screening framework used to identify this candidate (See superscript labels in Table 2 of the main manuscript), the Pourbaix formation energy ( $E_{PBX}$ ), energy above hull ( $E_{hull}$ ), and material cost. Entries are sorted by  $E_{PBX}$ .

Formula	Space group	# facets	$\eta$ (V)	Screening framework	$E_{PBX}$ (eV)	$E_{hull}$ (eV)	Cost (\$/kg)
HgSeO <sub>4</sub>	$Pmn2_1$	2	0.18	a,d,e,h,i,l,m,p	0.00	0.00	65.47
Ni(BiO <sub>3</sub> ) <sub>2</sub>	$P4_2/mnm$	4	0.36	a,b,c,d,e,f,g,h i,j,k,l,m,n,o,p	0.00	0.00	20.88
Na <sub>2</sub> Se <sub>2</sub> O <sub>7</sub>	$P\bar{1}$	2	0.21	a,d,e,h,i,l,m,p	0.00	0.00	110.43
Ag <sub>3</sub> O <sub>4</sub>	$P2_1/c$	4	0.33	a,b,c,d,e,f,g,h i,j,k,l,m,n,o,p	0.00	0.00	714.77
PbO <sub>2</sub>	$P4_2/mnm$	2	0.33	a,d,e,h,i,l,m,p	0.00	0.00	2.41
Mg(BiO <sub>3</sub> ) <sub>2</sub>	$P4_2/mnm$	3	0.52	a,b,c,d,e,f,g,h i,j,k,l,m,n,o,p	0.00	0.00	20.41
AgO	$Cccm$	2	0.49	a,d,e,h,i,l,m,p	0.00	0.00	745.41
AgO	$C2/c$	2	0.51	a,d,e,h,i,l,m,p	0.01	0.01	745.41
PbO <sub>2</sub>	$Pbcn$	2	0.56	a,b,c,d,e,f,g,h i,j,k,l,m,n,o,p	0.01	0.01	2.41
Co(BiO <sub>3</sub> ) <sub>2</sub>	$P4_2/mnm$	2	0.33	a,d,e,h,i,l,m,p	0.02	0.02	24.34
AgO	$P2_1/c$	3	0.50	a,b,c,d,e,f,g,h i,j,k,l,m,n,o,p	0.04	0.04	745.41
Bi <sub>4</sub> O <sub>7</sub>	$P\bar{1}$	2	0.22	a,d,e,h,i,l,m,p	0.04	0.00	22.67
FeCo <sub>9</sub> O <sub>20</sub>	$P\bar{1}$	4	0.41	a,b,c,d,e,f,g,h i,j,k,l,m,n,o,p	0.06	0.07	31.63
Ag <sub>2</sub> SeO <sub>4</sub>	$Fddd$	2	0.40	a,b,c,d,e,f,g,h i,j,k,l,m,n,o,p	0.07	0.00	547.23
Bi <sub>3</sub> SbO <sub>7</sub>	$P\bar{1}$	6	0.40	a,b,c,d,e,f,g,h i,j,k,l,m,n,o,p	0.07	0.00	20.85
CaBi <sub>4</sub> O <sub>9</sub>	$P2/c$	2	0.37	a,d,e,h,i,l,m,p	0.07	0.00	21.36
Li(CoO <sub>2</sub> ) <sub>8</sub>	$P\bar{1}$	4	0.46	a,b,c,d,e,f,g,h i,j,k,l,m,n,o,p	0.08	0.03	34.60
LiSbO <sub>3</sub>	$Pnna$	2	0.61	a,b,c,d,e,f,g,h i,j,k,l,m,n,o,p	0.09	0.00	10.82
CoAgO <sub>3</sub>	$R\bar{3}$	2	0.31	a,b,c,d,e,f,g,h i,j,k,l,m,n,o,p	0.09	0.09	444.63
AgSnO <sub>3</sub>	$Cmmm$	2	0.49	a,d,e,h,i,l,m,p	0.09	0.09	350.79



Table 4: Summary of screening criteria for our final set of candidates (continued).

Formula	Space group	# facets	$\eta$ (V)	Screening framework	$E_{PBX}$ (eV)	$E_{hull}$ (eV)	Cost (\$/kg)
Na(CoO <sub>2</sub> ) <sub>3</sub>	<i>C2/m</i>	3	0.42	a,b,c,d,e,f,g,h i,j,k,l,m,n,o,p	0.10	0.00	51.61
Ce <sub>9</sub> YO <sub>20</sub>	<i>P1</i>	2	0.71	a,d,e,h,i,l,m,p	0.10	0.02	266.60
Ce <sub>4</sub> SnO <sub>10</sub>	<i>R3m</i>	2	0.59	a,b,c,d,e,f,g,h i,j,k,l,m,n,o,p	0.11	0.07	239.03
Ag <sub>6</sub> Mo <sub>10</sub> O <sub>33</sub>	<i>P1</i>	3	0.55	a,d,e,h,i,l,m,p	0.11	0.02	278.69
CdGe <sub>2</sub> O <sub>5</sub>	<i>P1</i>	2	0.42	a,d,e,h,i,l,m,p	0.11	0.01	625.43
CuMoO <sub>4</sub>	<i>P1</i>	6	0.46	a,b,c,d,e,f,g,h i,j,k,l,m,n,o,p	0.13	0.02	21.29
ReAgO <sub>4</sub>	<i>I4<sub>1</sub>/a</i>	2	0.49	a,d,e,h,i,l,m,p	0.13	0.00	1737.20
CuMoO <sub>4</sub>	<i>P1</i>	3	0.63	a,b,c,d,e,f,g,h i,j,k,l,m,n,o,p	0.15	0.04	21.29
Ce <sub>2</sub> Mo <sub>4</sub> O <sub>15</sub>	<i>P1</i>	4	0.46	a,b,c,d,e,f,g,h i,j,k,l,m,n,o,p	0.16	0.02	126.84
Ca(CuO <sub>2</sub> ) <sub>2</sub>	<i>Pbcm</i>	2	0.60	a,b,c,d,e,f,g,h i,j,k,l,m,n,o,p	0.16	0.02	6.91
Cu <sub>3</sub> Mo <sub>2</sub> O <sub>9</sub>	<i>P1</i>	2	0.55	a,d,e,h,i,l,m,p	0.18	0.03	19.31
Ti <sub>2</sub> CoO <sub>5</sub>	<i>Cmcm</i>	2	0.58	a,b,c,d,e,f,g,h i,j,k,l,m,n,o,p	0.19	0.00	18.83
TlCoO <sub>3</sub>	<i>R3</i>	2	0.41	a,b,c,d,e,f,g,h i,j,k,l,m,n,o,p	0.19	0.05	3950.09
Mn(SbO <sub>3</sub> ) <sub>2</sub>	<i>P321</i>	2	0.48	a,b,c,d,e,f,g,h i,j,k,l,m,n,o,p	0.20	0.00	9.84
CuWO <sub>4</sub>	<i>P1</i>	2	0.39	a,b,c,d,e,f,g,h i,j,k,l,m,n,o,p	0.20	0.08	23.40
NiBiO <sub>3</sub>	<i>Pnma</i>	2	0.50	a,b,c,d,e,f,g,h i,j,k,l,m,n,o,p	0.21	0.04	20.66
Fe(Bi <sub>5</sub> O <sub>8</sub> ) <sub>5</sub>	<i>P23</i>	2	0.70	a,d,e,h,i,l,m,p	0.21	0.03	22.66
Cu <sub>3</sub> (SbO <sub>3</sub> ) <sub>4</sub>	<i>Im3</i>	2	0.37	a,d,e,h,i,l,m,p	0.21	0.02	10.76
Bi <sub>2</sub> O <sub>3</sub>	<i>P2<sub>1</sub>/c</i>	2	0.52	a,d,e,h,i,l,m,p	0.22	0.00	23.01
Cr <sub>2</sub> Ag <sub>2</sub> O <sub>7</sub>	<i>P1</i>	3	0.52	a,b,c,d,e,f,g,h i,j,k,l,m,n,o,p	0.22	0.02	430.56
Cr <sub>2</sub> Ag <sub>2</sub> O <sub>7</sub>	<i>P1</i>	3	0.43	a,b,c,d,e,f,g,h i,j,k,l,m,n,o,p	0.22	0.03	430.56
AlTiO <sub>3</sub>	<i>Pnma</i>	2	0.55	a,b,c,d,e,f,g,h i,j,k,l,m,n,o,p	0.22	0.08	4391.10
LiAgO <sub>2</sub>	<i>C2/m</i>	2	0.39	a,d,e,h,i,l,m,p	0.22	0.02	629.44

Table 5: Summary of screening criteria for our final set of candidates (continued).

Formula	Space group	# facets	$\eta$ (V)	Screening framework	$E_{PBX}$ (eV)	$E_{hull}$ (eV)	Cost (\$/kg)
Nb <sub>2</sub> Cu <sub>3</sub> O <sub>8</sub>	$P\bar{1}$	3	0.36	a,b,c,d,e,f,g,h i,j,k,l,m,n,o,p	0.23	-7.61	19.94
Cd(CoO <sub>2</sub> ) <sub>2</sub>	$Pm\bar{m}n$	2	0.43	a,b,c,d,e,f,g,h i,j,k,l,m,n,o,p	0.23	-6.26	22.61
Bi <sub>2</sub> O <sub>3</sub>	$Pbcn$	3	0.40	a,b,c,d,e,f,g,h i,j,k,l,m,n,o,p	0.24	0.02	23.01
Ag <sub>2</sub> BiO <sub>3</sub>	$Pnna$	3	0.34	a,b,c,d,e,f,g,h i,j,k,l,m,n,o,p	0.24	0.00	401.94
K(CoO <sub>2</sub> ) <sub>2</sub>	$P2_1$	3	0.51	a,b,c,d,e,f,g,h i,j,k,l,m,n,o,p	0.24	0.00	205.67
ZnCoO <sub>3</sub>	$C2/c$	2	0.49	a,d,e,h,i,l,m,p	0.25	0.06	19.81
Li(Bi <sub>3</sub> O <sub>5</sub> ) <sub>4</sub>	$I23$	2	0.47	a,d,e,h,i,l,m,p	0.25	0.08	22.74
CoAgO <sub>2</sub>	$P6_3/mmc$	2	0.47	a,b,c,d,e,f,g,h i,j,k,l,m,n,o,p	0.26	0.00	480.17
Cu(BiO <sub>2</sub> ) <sub>2</sub>	$P4/ncc$	3	0.41	a,b,c,d,e,f,g,h i,j,k,l,m,n,o,p	0.26	0.01	20.85
CdCoO <sub>3</sub>	$C2/c$	2	0.46	a,d,e,h,i,l,m,p	0.28	0.05	16.08
Cd <sub>2</sub> PbO <sub>4</sub>	$Pbam$	3	0.22	a,b,c,d,e,f,g,h i,j,k,l,m,n,o,p	0.29	0.00	2.59
Ag <sub>2</sub> GeO <sub>3</sub>	$P2_12_12_1$	2	0.62	a,d,e,h,i,l,m,p	0.29	0.00	862.25
MnMoO <sub>5</sub>	$P\bar{1}$	2	0.56	a,d,e,h,i,l,m,p	0.30	-8.27	18.68
ScCoO <sub>3</sub>	$P2_1/c$	2	0.34	a,b,c,d,e,f,g,h i,j,k,l,m,n,o,p	0.30	0.06	1045.31
Mn(SeO <sub>3</sub> ) <sub>2</sub>	$P2_1/c$	4	0.35	a,b,c,d,e,f,g,h i,j,k,l,m,n,o,p	0.31	0.00	75.94
Cr <sub>3</sub> AgO <sub>8</sub>	$C2/m$	2	0.62	a,b,c,d,e,f,g,h i,j,k,l,m,n,o,p	0.32	0.00	240.23
InCoO <sub>3</sub>	$Pnma$	2	0.58	a,b,c,d,e,f,g,h i,j,k,l,m,n,o,p	0.32	0.07	387.34
Ca(FeO <sub>2</sub> ) <sub>2</sub>	$Pm$	2	0.59	a,d,e,h,i,l,m,p	0.33	0.01	1.90
MnO <sub>2</sub>	$Pnma$	2	0.41	a,b,c,d,i,j,k,l	0.33	0.00	2.41
TiAg <sub>2</sub> O <sub>3</sub>	$C2/c$	2	0.47	a,d,e,h,i,l,m,p	0.33	0.04	594.55
CoPbO <sub>3</sub>	$R\bar{3}$	3	0.36	a,d,e,h,i,l,m,p	0.34	0.03	11.78
CaBiO <sub>3</sub>	$P2_1/c$	3	0.35	a,b,c,d,e,f,g,h i,j,k,l,m,n,o,p	0.34	0.00	18.94
Tl <sub>3</sub> Co <sub>3</sub> O <sub>8</sub>	$P1$	2	0.50	a,d,e,h,i,l,m,p	0.35	0.07	4018.88

Table 6: Summary of screening criteria for our final set of candidates (continued).

Formula	Space group	# facets	$\eta$ (V)	Screening framework	$E_{PBX}$ (eV)	$E_{hull}$ (eV)	Cost (\$/kg)
SrBiO <sub>3</sub>	$P2_1/c$	3	0.39	a,b,c,d,e,f,g,h i,j,k,l,m,n,o,p	0.35	0.00	16.06
Ce <sub>11</sub> O <sub>20</sub>	$P\bar{1}$	4	0.32	a,b,c,d,e,f,g,h i,j,k,l,m,n,o,p	0.35	0.00	290.42
NaBi <sub>5</sub> O <sub>8</sub>	$P\bar{1}$	3	0.52	a,b,c,d,e,f,g,h i,j,k,l,m,n,o,p	0.35	0.03	27.24
TlBiO <sub>4</sub>	$Cmmm$	2	0.33	a,d,i,l	0.36	-5.53	2580.81
Cu <sub>4</sub> Se <sub>3</sub> O <sub>10</sub>	$P\bar{1}$	2	0.52	a,d,e,h,i,l,m,p	0.36	0.02	57.57
BaBiO <sub>3</sub>	$P2_1/c$	2	0.63	a,d,e,h,i,l,m,p	0.36	0.00	13.87
Ce <sub>2</sub> (GeO <sub>3</sub> ) <sub>3</sub>	$P\bar{1}$	2	0.55	a,b,c,d,e,f,g,h i,j,k,l,m,n,o,p	0.36	0.05	645.52
CdSe <sub>2</sub> O <sub>5</sub>	$C2/c$	2	0.66	a,d,e,h,i,l,m,p	0.36	0.00	67.37
AgBiO <sub>2</sub>	$P2_1/m$	3	0.55	a,b,c,d,e,f,g,h i,j,k,l,m,n,o,p	0.36	0.00	279.98
Zn(BiO <sub>2</sub> ) <sub>2</sub>	$P\bar{1}$	3	0.43	a,b,c,d,e,f,g,h i,j,k,l,m,n,o,p	0.36	0.07	20.03
CuSeO <sub>3</sub>	$P2_1/c$	4	0.41	a,b,c,d,e,f,g,h i,j,k,l,m,n,o,p	0.37	0.03	64.44
Cu <sub>2</sub> SeO <sub>4</sub>	$P2_1/c$	4	0.38	a,b,c,d,e,f,g,h i,j,k,l,m,n,o,p	0.37	0.03	47.88
CdSeO <sub>3</sub>	$Pnma$	4	0.49	a,b,c,d,e,f,g,h i,j,k,l,m,n,o,p	0.37	0.01	50.04
FeSnO <sub>3</sub>	$P\bar{1}$	2	0.51	a,b,c,d,e,f,g,h i,j,k,l,m,n,o,p	0.38	0.00	18.17
CoGeO <sub>3</sub>	$C2/c$	3	0.50	a,b,c,d,e,f,g,h i,j,k,l,m,n,o,p	0.38	0.06	604.48
Hg <sub>2</sub> MoO <sub>4</sub>	$C2/c$	2	0.26	a,d,e,h,i,l,m,p	0.38	0.01	45.80
CdIn <sub>2</sub> O <sub>4</sub>	$Imma$	2	0.46	a,b,c,d,e,f,g,h i,j,k,l,m,n,o,p	0.38	0.08	408.44
BaTl <sub>2</sub> O <sub>4</sub>	$Pnma$	3	0.54	a,b,c,d,e,f,g,h i,j,k,l,m,n,o,p	0.38	0.00	4021.08
Cr(SbO <sub>3</sub> ) <sub>2</sub>	$Pnnm$	2	0.39	a,b,c,d,e,f,g,h i,j,k,l,m,n,o,p	0.38	0.06	10.88
Li <sub>3</sub> BiO <sub>4</sub>	$P2/c$	2	0.41	a,b,c,d,i,j,k,l	0.38	0.00	18.93
SrSe <sub>2</sub> O <sub>5</sub>	$P\bar{1}$	3	0.25	a,b,c,d,e,f,g,h i,j,k,l,m,n,o,p	0.39	0.00	71.87
Ca <sub>2</sub> Se <sub>3</sub> O <sub>8</sub>	$P\bar{1}$	2	0.70	a,d,e,h,i,l,m,p	0.39	0.00	79.44

Table 7: Summary of screening criteria for our final set of candidates (continued).

Formula	Space group	# facets	$\eta$ (V)	Screening framework	$E_{PBX}$ (eV)	$E_{hull}$ (eV)	Cost (\$/kg)
$\text{Cd}_6(\text{CoO}_3)_5$	$R\bar{3}2$	2	0.39	a,b,c,d,e,f,g,h i,j,k,l,m,n,o,p	0.39	0.09	14.84
$\text{Ag}_2\text{SeO}_3$	$P2_1/c$	3	0.29	a,b,c,d,g,h,i,j k,l,o,p	0.40	0.00	572.64
$\text{BaSe}_2\text{O}_5$	$P2_1/c$	2	0.66	a,d,e,h,i,l,m,p	0.40	0.00	62.17
$\text{LuCoO}_3$	$Pnma$	2	0.56	a,b,c,d,e,f,g,h i,j,k,l,m,n,o,p	0.40	0.03	4666.55
$\text{Ag}_4\text{GeO}_4$	$P\bar{1}$	6	0.52	a,b,c,d,e,f,g,h i,j,k,l,m,n,o,p	0.40	0.01	835.50
$\text{CuReO}_4$	$P\bar{1}$	4	0.33	a,b,c,d,e,f,g,h i,j,k,l,m,n,o,p	0.40	0.06	1690.40
$\text{Co}_{11}\text{CuO}_{16}$	$P2/m$	2	0.56	a,d,i,l	0.40	0.06	36.39
$\text{CoSe}_2\text{O}_5$	$Pbcn$	2	0.40	a,b,c,d	0.41	0.00	88.84
$\text{Co}_5\text{SbO}_8$	$R\bar{3}m$	2	0.49	a,b,c,d,i,j,k,l	0.41	0.00	32.16
$\text{NaTlO}_2$	$I4_1/amd$	2	0.49	a,d,e,h,i,l,m,p	0.41	0.02	4751.26
$\text{MgIn}_2\text{O}_4$	$Imma$	2	0.42	a,b,c,d,e,f,g,h i,j,k,l,m,n,o,p	0.41	0.02	521.03
$\text{Li}_7\text{Co}_5\text{O}_{12}$	$C2/m$	4	0.38	a,b,c,d,e,f,g,h i,j,k,l,m,n,o,p	0.41	0.03	30.17
$\text{Hg}_2\text{WO}_4$	$C2/c$	2	0.68	a,d,e,h,i,l,m,p	0.42	0.00	43.49
$\text{CuReO}_4$	$P\bar{1}$	3	0.56	a,b,c,d,e,f,g,h i,j,k,l,m,n,o,p	0.42	0.08	1690.40
$\text{Sn}_2\text{Ge}_2\text{O}_7$	$P\bar{1}$	2	0.55	a,d,e,h,i,l,m,p	0.42	0.06	442.22
$\text{MnTlO}_3$	$Pnma$	5	0.20	a,b,c,d,i,j,k,l	0.42	0.05	3991.79
$\text{Ag}_2\text{HgO}_2$	$P4_32_12$	3	0.47	a,b,c,d,g,h,i,j k,l,o,p	0.43	0.00	435.93
$\text{Co}_2\text{NiO}_4$	$Imma$	2	0.50	a,b,c,d,e,f,g,h i,j,k,l,m,n,o,p	0.43	0.09	30.91
$\text{Ba}_8(\text{Bi}_2\text{O}_7)_3$	$P\bar{1}$	6	0.46	a,b,c,d,i,j,k,l	0.43	0.00	12.29
$\text{AgSbO}_4$	$Cmmm$	3	0.32	a,b,c,d,i,j,k,l	0.44	-5.61	320.88
$\text{MnTlO}_3$	$P\bar{1}$	3	0.36	a,b,c,d,i,j,k,l	0.44	0.07	3991.79
$\text{Ca}(\text{CoO}_2)_2$	$Pnma$	2	0.32	a,b,c,d,e,f,g,h i,j,k,l,m,n,o,p	0.44	0.00	29.47
$\text{Tl}_2\text{SeO}_4$	$Pnma$	3	0.58	a,b,c,d,i,j,k,l	0.45	0.00	4467.30
$\text{Tl}_2\text{SeO}_4$	$P2_12_12_1$	4	0.52	a,b,c,d,i,j,k,l	0.45	0.00	4467.30
$\text{CaSeO}_3$	$Pnma$	2	0.60	a,b,c,d,g,h,i,j k,l,o,p	0.45	0.01	71.04

Table 8: Summary of screening criteria for our final set of candidates (continued).

Formula	Space group	# facets	$\eta$ (V)	Screening framework	$E_{PBX}$ (eV)	$E_{hull}$ (eV)	Cost (\$/kg)
$\text{CdCu}_2\text{O}_3$	$Pm\bar{m}n$	2	0.50	a,b,c,d,g,h,i,j k,l,o,p	0.46	0.04	5.78
$\text{CuSbO}_4$	$Cmmm$	2	0.36	a,b,c,d,i,j,k,l	0.47	-6.01	10.18
$\text{YMn}_2\text{O}_5$	$Pbam$	2	0.54	a,b,c,d,i,j,k,l	0.47	0.00	11.56
$\text{Cu}_2\text{W}_2\text{O}_7$	$P\bar{1}$	2	0.43	a,b,c,d,i,j,k,l	0.47	0.10	23.94
$\text{Ca}_3\text{WO}_6$	$P2_1/c$	2	0.49	a,d,e,h,i,l,m,p	0.47	0.02	18.40
$\text{YCoO}_3$	$P2_1/c$	2	0.52	a,b,c,d,i,j,k,l	0.48	0.01	30.52
$\text{ZnCu}_2\text{O}_3$	$Pm\bar{m}n$	3	0.42	a,b,c,d,g,h,i,j k,l,o,p	0.48	0.10	6.44
$\text{CuNiO}_2$	$C2/m$	2	0.40	a,b,c,d,i,j,k,l	0.49	0.07	11.60
$\text{MnBiO}_3$	$Pnma$	3	0.51	a,b,c,d,k,l	0.50	0.03	17.78

Table 9: Summary of screening criteria for our final set of candidates (continued). All materials listed from here are unstable as bulk materials ( $E_{PBX} > 0.5$  eV) but can be stabilized as nanoparticles.

Formula	Space group	# facets	$\eta$ (V)	Screening framework	$E_{PBX}$ (eV)	$E_{hull}$ (eV)	Cost (\$/kg)
Cr <sub>2</sub> WO <sub>6</sub>	$P4_2/mnm$	2	0.25	c,d,k,l	0.52	0.00	20.20
TlCuO <sub>2</sub>	$R\bar{3}m$	2	0.43	h,p	0.52	0.05	4091.65
Y(FeO <sub>2</sub> ) <sub>2</sub>	$P\bar{1}$	2	0.53	c,d,g,h,k,l,o,p	0.54	0.01	11.23
Sr <sub>2</sub> Tl <sub>2</sub> O <sub>5</sub>	$P2_1/c$	2	0.37	k,l	0.55	0.00	3694.92
ZrCoO <sub>3</sub>	$P\bar{1}$	3	0.46	c,d,g,h,k,l,o,p	0.55	0.10	32.83
TiVO <sub>4</sub>	$P2_1$	2	0.58	c,d,k,l	0.56	0.02	120.33
HfFeO <sub>3</sub>	$Pnma$	2	0.53	c,d,k,l	0.56	0.06	569.53
Mn <sub>4</sub> CuO <sub>8</sub>	$C2/m$	3	0.39	d,l	0.56	0.07	3.51
CoCu <sub>2</sub> O <sub>3</sub>	$Pmnm$	3	0.42	c,d,k,l	0.57	0.07	18.94
MnSe <sub>2</sub> O <sub>5</sub>	$Pbcn$	2	0.50	c,d,k,l	0.58	0.00	79.93
CrMoO <sub>4</sub>	$Cmmm$	2	0.42	c,d,k,l	0.59	0.00	21.89
KMn <sub>2</sub> O <sub>4</sub>	$P\bar{1}$	2	0.47	d,l	0.60	0.00	185.55
Ba <sub>2</sub> Tl <sub>2</sub> O <sub>5</sub>	$Pnma$	2	0.34	d,l	0.60	0.00	3213.59
LuMnO <sub>3</sub>	$Pnma$	3	0.54	c,d,g,h,k,l,o,p	0.61	0.05	4722.98
TiMnO <sub>3</sub>	$R\bar{3}$	2	0.28	d,l	0.62	0.00	5.36
KBiO <sub>2</sub>	$C2/c$	2	0.27	c,d,k,l	0.62	0.00	158.83
Na <sub>5</sub> ReO <sub>6</sub>	$C2/m$	2	0.30	h,l,p	0.62	0.00	1406.49
CuTeO <sub>4</sub>	$Cmmm$	3	0.54	c,d,k,l	0.63	-5.71	177.66
ScCrO <sub>3</sub>	$Pnma$	2	0.46	c,d,g,h,k,l,o,p	0.63	0.04	1077.47
Ta <sub>2</sub> CrO <sub>6</sub>	$P4_2/mnm$	2	0.56	c,d,k,l	0.64	0.01	109.26
MnSnO <sub>3</sub>	$R\bar{3}$	2	0.43	c,d,k,l	0.65	0.00	18.71
Li <sub>4</sub> PbO <sub>4</sub>	$Cmcm$	2	0.66	d,l	0.65	0.00	2.61
VSbO <sub>4</sub>	$Cmmm$	2	0.44	d,h,l,p	0.66	0.02	87.80
ScCuO <sub>2</sub>	$R\bar{3}m$	2	0.41	d,h,l,p	0.66	0.00	1112.09
Mn <sub>2</sub> BeO <sub>4</sub>	$Pnma$	3	0.32	c,d,g,h,k,l,o,p	0.66	0.04	24.36
AlCuO <sub>2</sub>	$P6_3/mmc$	2	0.48	c,d,k,l,o,p	0.67	0.00	6.28
TiCu <sub>3</sub> O <sub>4</sub>	$P2_1/c$	2	0.38	g,h,o,p	0.68	0.07	8.46
Ag <sub>2</sub> PbO <sub>2</sub>	$C2/c$	3	0.43	g,h,o,p	0.70	0.00	406.97
LuCrO <sub>3</sub>	$Pnma$	2	0.43	c,d,g,h,k,l,o,p	0.71	0.00	4774.87
VSeO <sub>4</sub>	$P2_1/c$	2	0.46	d,l	0.72	0.00	157.65
Ag <sub>3</sub> RuO <sub>4</sub>	$P4_122$	2	0.60	d,l	0.72	0.07	5554.14
GePb <sub>5</sub> O <sub>7</sub>	$Pbca$	2	0.68	g,h,k,l,o,p	0.72	0.01	88.53
VCrO <sub>4</sub>	$Cmcm$	2	0.32	c,d	0.73	0.01	116.99
TlTeO <sub>4</sub>	$Cmmm$	2	0.50	c,d,k,l	0.74	-5.50	3210.31
MnSeO <sub>3</sub>	$P2_1/c$	2	0.44	c,d,k,l	0.75	0.00	64.79
Li <sub>3</sub> BiO <sub>3</sub>	$P\bar{1}$	2	0.52	d,h,l,p	0.75	0.00	19.85
VZn <sub>2</sub> O <sub>4</sub>	$Imma$	2	0.47	k,l	0.75	0.02	79.05
Fe <sub>10</sub> O <sub>11</sub>	$P\bar{1}$	3	0.50	g,h,o,p	0.77	0.05	0.88

Table 10: Summary of screening criteria for our final set of candidates (continued).

Formula	Space group	# facets	$\eta$ (V)	Screening framework	$E_{PBX}$ (eV)	$E_{hull}$ (eV)	Cost (\$/kg)
Tl <sub>2</sub> SnO <sub>3</sub>	<i>Pnma</i>	2	0.60	d,h	0.80	0.00	4269.57
ScMn <sub>2</sub> O <sub>4</sub>	<i>C2/m</i>	3	0.29	k,l	0.84	0.03	712.73
ZrMnO <sub>3</sub>	<i>R<math>\bar{3}</math></i>	2	0.50	c,d,g,h,k,l,o,p	0.84	0.03	18.24
Li(CuO) <sub>2</sub>	<i>Pnma</i>	2	0.52	k,l	0.85	0.00	8.03
Fe <sub>17</sub> O <sub>18</sub>	<i>P<math>\bar{1}</math></i>	2	0.52	l	0.86	0.04	0.86
K <sub>6</sub> Co <sub>2</sub> O <sub>7</sub>	<i>P2<sub>1</sub>/c</i>	4	0.36	c,d,k,l	0.87	0.00	519.06
Cr <sub>2</sub> NiO <sub>4</sub>	<i>P1</i>	3	0.38	d,h,l,p	0.88	0.04	9.96
YCuO <sub>2</sub>	<i>P6<sub>3</sub>/mmc</i>	2	0.38	k,l	0.94	0.00	18.75
Mn <sub>2</sub> SnO <sub>4</sub>	<i>Imma</i>	3	0.42	c,d,g,h,k,l,o,p	0.94	0.00	14.72
MnCuO <sub>2</sub>	<i>P<math>\bar{1}</math></i>	2	0.58	l	0.94	0.00	5.41
YCuO <sub>2</sub>	<i>R<math>\bar{3}m</math></i>	2	0.38	g,h,o,p	0.94	0.00	18.75
Mn <sub>23</sub> FeO <sub>32</sub>	<i>P<math>\bar{1}</math></i>	2	0.28	d,h,l,p	0.95	0.01	2.27
SrCr <sub>2</sub> O <sub>4</sub>	<i>Pmmm</i>	3	0.62	c,d,k,l	0.98	0.00	4.97
KSnO <sub>2</sub>	<i>P<math>\bar{1}</math></i>	2	0.19	c,d,g,h,k,l,o,p	0.98	0.02	226.98
CdRuO <sub>4</sub>	<i>Cmmm</i>	2	0.53	d,l	0.99	-6.31	8784.84
Co(SbO <sub>2</sub> ) <sub>2</sub>	<i>P4<sub>2</sub>/mbc</i>	2	0.66	k,l	0.99	0.00	18.42
Mn <sub>2</sub> CrO <sub>4</sub>	<i>Cc</i>	2	0.37	c,d,k,l	1.04	0.00	4.02
Na <sub>2</sub> Sb <sub>4</sub> O <sub>7</sub>	<i>C2/c</i>	2	0.35	k,l	1.05	0.00	29.14
CeCrO <sub>3</sub>	<i>Pnma</i>	2	0.29	c,d,g,h,k,l,o,p	1.05	0.05	206.93
Na <sub>2</sub> Co <sub>2</sub> O <sub>3</sub>	<i>P2<sub>1</sub>/c</i>	4	0.30	g,h,o,p	1.07	0.00	83.99
NaSb <sub>5</sub> O <sub>8</sub>	<i>P<math>\bar{1}</math></i>	3	0.52	k,l	1.09	0.00	19.53
RuPbO <sub>4</sub>	<i>Cmmm</i>	2	0.64	d,l	1.12	-6.84	6548.46
SnRuO <sub>4</sub>	<i>Cmmm</i>	2	0.32	c,d,k,l	1.14	-7.30	8602.47
Ti(SnO <sub>2</sub> ) <sub>2</sub>	<i>P4<sub>2</sub>/mbc</i>	2	0.48	k,l	1.15	0.00	24.39
LiMn <sub>3</sub> O <sub>4</sub>	<i>P<math>\bar{1}</math></i>	2	0.63	d,l	1.26	0.02	2.37
K <sub>2</sub> PbO <sub>2</sub>	<i>P<math>\bar{1}</math></i>	2	0.55	k,l	1.31	0.00	248.19
Mn <sub>2</sub> NiO <sub>3</sub>	<i>Immm</i>	2	0.47	d,h,l,p	1.34	0.08	6.73
Mn <sub>3</sub> NiO <sub>4</sub>	<i>Cmmm</i>	2	0.54	d,l	1.44	0.09	5.63
BaMn <sub>2</sub> O <sub>3</sub>	<i>Immm</i>	2	0.62	k,l	1.66	0.00	1.38
CaMn <sub>7</sub> O <sub>8</sub>	<i>C2/m</i>	2	0.48	l	1.66	0.03	2.48

## 7 Candidate materials literature references

Table 11: Overpotentials from OC22, the experimental literature, and DFT (see Figure 7(b) in the main manuscript) along with the PDS for our final set of 190 candidate catalyst materials for OER across all screening frameworks. Experimental results are reported for systems containing similar chemical systems and do not necessarily reflect the same formula of the candidate catalyst. Candidates are listed in the same order as Tables S3-10 (from lowest to highest  $E_{PBX}$ ).

Formula	$\eta$ (V) (OC22)	$\eta$ (V) (exp.)	$\eta$ (V) (DFT)	PDS
HgSeO <sub>4</sub>	0.176		0.217	OH $\longrightarrow$ O <sup>*+</sup> H <sup>+</sup>
Ni(BiO <sub>3</sub> ) <sub>2</sub>	0.361	0.300 <sup>85</sup>		OH $\longrightarrow$ O <sup>*+</sup> H <sup>+</sup>
Na <sub>2</sub> Se <sub>2</sub> O <sub>7</sub>	0.208		0.741	OH $\longrightarrow$ O <sup>*+</sup> H <sup>+</sup>
Ag <sub>3</sub> O <sub>4</sub>	0.333	0.37 <sup>61</sup>		OH $\longrightarrow$ O <sup>*+</sup> H <sup>+</sup>
PbO <sub>2</sub>	0.334			OH $\longrightarrow$ O <sup>*+</sup> H <sup>+</sup>
Mg(BiO <sub>3</sub> ) <sub>2</sub>	0.525			OH $\longrightarrow$ O <sup>*+</sup> H <sup>+</sup>
AgO	0.495	0.37 <sup>61</sup>		H <sub>2</sub> O <sup>+</sup> O <sup>*</sup> $\longrightarrow$ OOH <sup>*+</sup> H <sup>+</sup>
AgO	0.513	0.37 <sup>61</sup>		H <sub>2</sub> O <sup>+</sup> O <sup>*</sup> $\longrightarrow$ OOH <sup>*+</sup> H <sup>+</sup>
PbO <sub>2</sub>	0.561			H <sub>2</sub> O <sup>+</sup> O <sup>*</sup> $\longrightarrow$ OOH <sup>*+</sup> H <sup>+</sup>
Co(BiO <sub>3</sub> ) <sub>2</sub>	0.331	0.320 <sup>86</sup>		OH $\longrightarrow$ O <sup>*+</sup> H <sup>+</sup>
AgO	0.496	0.37 <sup>61</sup>		H <sub>2</sub> O <sup>+</sup> O <sup>*</sup> $\longrightarrow$ OOH <sup>*+</sup> H <sup>+</sup>
Bi <sub>4</sub> O <sub>7</sub>	0.221	0.800 <sup>87</sup>	0.353	OH $\longrightarrow$ O <sup>*+</sup> H <sup>+</sup>
FeCo <sub>9</sub> O <sub>20</sub>	0.412	0.408, <sup>75</sup> 0.412 <sup>74</sup>		H <sub>2</sub> O <sup>+</sup> O <sup>*</sup> $\longrightarrow$ OOH <sup>*+</sup> H <sup>+</sup>
Ag <sub>2</sub> SeO <sub>4</sub>	0.395	0.192 <sup>88</sup>		H <sub>2</sub> O <sup>+</sup> O <sup>*</sup> $\longrightarrow$ OOH <sup>*+</sup> H <sup>+</sup>
Bi <sub>3</sub> SbO <sub>7</sub>	0.398			OH $\longrightarrow$ O <sup>*+</sup> H <sup>+</sup>
CaBi <sub>4</sub> O <sub>9</sub>	0.368			OH $\longrightarrow$ O <sup>*+</sup> H <sup>+</sup>
Li(CoO <sub>2</sub> ) <sub>8</sub>	0.459	0.430 <sup>89</sup>		OH $\longrightarrow$ O <sup>*+</sup> H <sup>+</sup>
LiSbO <sub>3</sub>	0.611			H <sub>2</sub> O <sup>+</sup> O <sup>*</sup> $\longrightarrow$ OOH <sup>*+</sup> H <sup>+</sup>
CoAgO <sub>3</sub>	0.306	0.310 <sup>90</sup>		OH $\longrightarrow$ O <sup>*+</sup> H <sup>+</sup>
AgSnO <sub>3</sub>	0.491			OH $\longrightarrow$ O <sup>*+</sup> H <sup>+</sup>
Na(CoO <sub>2</sub> ) <sub>3</sub>	0.416	0.236 <sup>83</sup>		OH $\longrightarrow$ O <sup>*+</sup> H <sup>+</sup>
Ce <sub>9</sub> YO <sub>20</sub>	0.705			OH $\longrightarrow$ O <sup>*+</sup> H <sup>+</sup>
Ce <sub>4</sub> SnO <sub>10</sub>	0.594			H <sub>2</sub> O <sup>+</sup> O <sup>*</sup> $\longrightarrow$ OOH <sup>*+</sup> H <sup>+</sup>
Ag <sub>6</sub> Mo <sub>10</sub> O <sub>33</sub>	0.546	> 0.540 <sup>91</sup>		OH $\longrightarrow$ O <sup>*+</sup> H <sup>+</sup>
CdGe <sub>2</sub> O <sub>5</sub>	0.423			OH $\longrightarrow$ O <sup>*+</sup> H <sup>+</sup>
CuMoO <sub>4</sub>	0.460			OH $\longrightarrow$ O <sup>*+</sup> H <sup>+</sup>
ReAgO <sub>4</sub>	0.488			OH $\longrightarrow$ O <sup>*+</sup> H <sup>+</sup>
CuMoO <sub>4</sub>	0.626			OH $\longrightarrow$ O <sup>*+</sup> H <sup>+</sup>
Ce <sub>2</sub> Mo <sub>4</sub> O <sub>15</sub>	0.463			OH $\longrightarrow$ O <sup>*+</sup> H <sup>+</sup>
Ca(CuO <sub>2</sub> ) <sub>2</sub>	0.598			H <sub>2</sub> O <sup>+</sup> O <sup>*</sup> $\longrightarrow$ OOH <sup>*+</sup> H <sup>+</sup>
Cu <sub>3</sub> Mo <sub>2</sub> O <sub>9</sub>	0.545			OH $\longrightarrow$ O <sup>*+</sup> H <sup>+</sup>
Ti <sub>2</sub> CoO <sub>5</sub>	0.577	0.66 <sup>92</sup>		OH $\longrightarrow$ O <sup>*+</sup> H <sup>+</sup>



Table 12: Overpotentials from OC22, the experimental literature, and DFT (see Figure 7(b) in the main manuscript) along with the PDS for our final set of 190 candidate (continued).

Formula	$\eta$ (V) (OC22)	$\eta$ (V) (exp.)	$\eta$ (V) (DFT)	PDS
TlCoO <sub>3</sub>	0.407			H <sub>2</sub> O <sup>+</sup> O* $\longrightarrow$ OOH <sup>**</sup> H <sup>+</sup>
Mn(SbO <sub>3</sub> ) <sub>2</sub>	0.484	0.340 <sup>72</sup>		OOH* $\longrightarrow$ O <sub>2</sub> <sup>+</sup> H <sup>+</sup>
CuWO <sub>4</sub>	0.391	0.270 <sup>93</sup>		OH $\longrightarrow$ O <sup>*</sup> H <sup>+</sup>
NiBiO <sub>3</sub>	0.504	0.300 <sup>85</sup>		H <sub>2</sub> O <sup>+</sup> O* $\longrightarrow$ OOH <sup>**</sup> H <sup>+</sup>
Fe(Bi <sub>5</sub> O <sub>8</sub> ) <sub>5</sub>	0.699	0.420 <sup>94</sup>		H <sub>2</sub> O <sup>+</sup> O* $\longrightarrow$ OOH <sup>**</sup> H <sup>+</sup>
Cu <sub>3</sub> (SbO <sub>3</sub> ) <sub>4</sub>	0.366			OH $\longrightarrow$ O <sup>*</sup> H <sup>+</sup>
Bi <sub>2</sub> O <sub>3</sub>	0.524	0.800 <sup>87</sup>	0.292	OH $\longrightarrow$ O <sup>*</sup> H <sup>+</sup>
Cr <sub>2</sub> Ag <sub>2</sub> O <sub>7</sub>	0.522	> 0.540 <sup>91</sup>		H <sub>2</sub> O <sup>+</sup> O* $\longrightarrow$ OOH <sup>**</sup> H <sup>+</sup>
Cr <sub>2</sub> Ag <sub>2</sub> O <sub>7</sub>	0.426	> 0.540 <sup>91</sup>		H <sub>2</sub> O <sup>+</sup> O* $\longrightarrow$ OOH <sup>**</sup> H <sup>+</sup>
AlTlO <sub>3</sub>	0.553			OH $\longrightarrow$ O <sup>*</sup> H <sup>+</sup>
LiAgO <sub>2</sub>	0.388			OH $\longrightarrow$ O <sup>*</sup> H <sup>+</sup>
Nb <sub>2</sub> Cu <sub>3</sub> O <sub>8</sub>	0.363			OH $\longrightarrow$ O <sup>*</sup> H <sup>+</sup>
Cd(CoO <sub>2</sub> ) <sub>2</sub>	0.431			OH $\longrightarrow$ O <sup>*</sup> H <sup>+</sup>
Bi <sub>2</sub> O <sub>3</sub>	0.396	0.800 <sup>87</sup>		H <sub>2</sub> O <sup>+</sup> O* $\longrightarrow$ OOH <sup>**</sup> H <sup>+</sup>
Ag <sub>2</sub> BiO <sub>3</sub>	0.343	0.700 <sup>62</sup>		OH $\longrightarrow$ O <sup>*</sup> H <sup>+</sup>
K(CoO <sub>2</sub> ) <sub>2</sub>	0.510			OOH* $\longrightarrow$ O <sub>2</sub> <sup>+</sup> H <sup>+</sup>
ZnCoO <sub>3</sub>	0.488	< 0.400, <sup>95</sup> 0.390-0.480 <sup>96</sup>		OH $\longrightarrow$ O <sup>*</sup> H <sup>+</sup>
Li(Bi <sub>3</sub> O <sub>5</sub> ) <sub>4</sub>	0.473			OOH* $\longrightarrow$ O <sub>2</sub> <sup>+</sup> H <sup>+</sup>
CoAgO <sub>2</sub>	0.472	0.310 <sup>90</sup>		OH $\longrightarrow$ O <sup>*</sup> H <sup>+</sup>
Cu(BiO <sub>2</sub> ) <sub>2</sub>	0.406	0.530 <sup>97</sup>		H <sub>2</sub> O <sup>+</sup> O* $\longrightarrow$ OOH <sup>**</sup> H <sup>+</sup>
CdCoO <sub>3</sub>	0.459			OH $\longrightarrow$ O <sup>*</sup> H <sup>+</sup>
Cd <sub>2</sub> PbO <sub>4</sub>	0.220		0.222	OH $\longrightarrow$ O <sup>*</sup> H <sup>+</sup>
Ag <sub>2</sub> GeO <sub>3</sub>	0.616			OOH* $\longrightarrow$ O <sub>2</sub> <sup>+</sup> H <sup>+</sup>
MnMoO <sub>5</sub>	0.564	0.570 <sup>98</sup>		OH $\longrightarrow$ O <sup>*</sup> H <sup>+</sup>
ScCoO <sub>3</sub>	0.341			OH $\longrightarrow$ O <sup>*</sup> H <sup>+</sup>
Mn(SeO <sub>3</sub> ) <sub>2</sub>	0.349			OH $\longrightarrow$ O <sup>*</sup> H <sup>+</sup>
Cr <sub>3</sub> AgO <sub>8</sub>	0.620	> 0.540 <sup>91</sup>		H <sub>2</sub> O <sup>+</sup> O* $\longrightarrow$ OOH <sup>**</sup> H <sup>+</sup>
InCoO <sub>3</sub>	0.582	0.370 <sup>99</sup>		OH $\longrightarrow$ O <sup>*</sup> H <sup>+</sup>
Ca(FeO <sub>2</sub> ) <sub>2</sub>	0.586	0.320 <sup>100</sup>		OH $\longrightarrow$ O <sup>*</sup> H <sup>+</sup>
MnO <sub>2</sub>	0.406	> 0.600 <sup>77</sup>		OOH* $\longrightarrow$ O <sub>2</sub> <sup>+</sup> H <sup>+</sup>
TiAg <sub>2</sub> O <sub>3</sub>	0.468	0.650 <sup>101</sup>		H <sub>2</sub> O <sup>+</sup> O* $\longrightarrow$ OOH <sup>**</sup> H <sup>+</sup>
CoPbO <sub>3</sub>	0.356	0.560 <sup>102</sup>		OH $\longrightarrow$ O <sup>*</sup> H <sup>+</sup>
CaBiO <sub>3</sub>	0.352			OH $\longrightarrow$ O <sup>*</sup> H <sup>+</sup>
Tl <sub>3</sub> Co <sub>3</sub> O <sub>8</sub>	0.503			H <sub>2</sub> O <sup>+</sup> O* $\longrightarrow$ OOH <sup>**</sup> H <sup>+</sup>
SrBiO <sub>3</sub>	0.392			OH $\longrightarrow$ O <sup>*</sup> H <sup>+</sup>
Ce <sub>11</sub> O <sub>20</sub>	0.324	0.370 <sup>103</sup>		OOH* $\longrightarrow$ O <sub>2</sub> <sup>+</sup> H <sup>+</sup>

Table 13: Overpotentials from OC22, the experimental literature, and DFT (see Figure 7(b) in the main manuscript) along with the PDS for our final set of 190 candidate (continued).

Formula	$\eta$ (V) (OC22)	$\eta$ (V) (exp.)	$\eta$ (V) (DFT)	PDS
NaBi <sub>5</sub> O <sub>8</sub>	0.517		1.197	OOH* $\longrightarrow$ O <sub>2</sub> <sup>+</sup> H <sup>+</sup>
TlBiO <sub>4</sub>	0.333			OOH* $\longrightarrow$ O <sub>2</sub> <sup>+</sup> H <sup>+</sup>
Cu <sub>4</sub> Se <sub>3</sub> O <sub>10</sub>	0.520	0.440 <sup>104</sup>		OH $\longrightarrow$ O <sup>++</sup> H <sup>+</sup>
BaBiO <sub>3</sub>	0.631			OOH* $\longrightarrow$ O <sub>2</sub> <sup>+</sup> H <sup>+</sup>
Ce <sub>2</sub> (GeO <sub>3</sub> ) <sub>3</sub>	0.546			OH $\longrightarrow$ O <sup>++</sup> H <sup>+</sup>
CdSe <sub>2</sub> O <sub>5</sub>	0.659			OH $\longrightarrow$ O <sup>++</sup> H <sup>+</sup>
AgBiO <sub>2</sub>	0.548	0.700 <sup>62</sup>		OH $\longrightarrow$ O <sup>++</sup> H <sup>+</sup>
Zn(BiO <sub>2</sub> ) <sub>2</sub>	0.429			OH $\longrightarrow$ O <sup>++</sup> H <sup>+</sup>
CuSeO <sub>3</sub>	0.406	0.440 <sup>104</sup>		OH $\longrightarrow$ O <sup>++</sup> H <sup>+</sup>
Cu <sub>2</sub> SeO <sub>4</sub>	0.381	0.440 <sup>104</sup>		H <sub>2</sub> O <sup>+</sup> O* $\longrightarrow$ OOH <sup>++</sup> H <sup>+</sup>
CdSeO <sub>3</sub>	0.488			OOH* $\longrightarrow$ O <sub>2</sub> <sup>+</sup> H <sup>+</sup>
FeSnO <sub>3</sub>	0.512			OH $\longrightarrow$ O <sup>++</sup> H <sup>+</sup>
CoGeO <sub>3</sub>	0.496	0.340 <sup>105</sup>		OH $\longrightarrow$ O <sup>++</sup> H <sup>+</sup>
Hg <sub>2</sub> MoO <sub>4</sub>	0.259			OH $\longrightarrow$ O <sup>++</sup> H <sup>+</sup>
CdIn <sub>2</sub> O <sub>4</sub>	0.457			H <sub>2</sub> O <sup>+</sup> O* $\longrightarrow$ OOH <sup>++</sup> H <sup>+</sup>
BaTl <sub>2</sub> O <sub>4</sub>	0.544			H <sub>2</sub> O <sup>+</sup> O* $\longrightarrow$ OOH <sup>++</sup> H <sup>+</sup>
Cr(SbO <sub>3</sub> ) <sub>2</sub>	0.386			H <sub>2</sub> O <sup>+</sup> O* $\longrightarrow$ OOH <sup>++</sup> H <sup>+</sup>
Li <sub>3</sub> BiO <sub>4</sub>	0.414			OH $\longrightarrow$ O <sup>++</sup> H <sup>+</sup>
SrSe <sub>2</sub> O <sub>5</sub>	0.254			H <sub>2</sub> O <sup>+</sup> O* $\longrightarrow$ OOH <sup>++</sup> H <sup>+</sup>
Ca <sub>2</sub> Se <sub>3</sub> O <sub>8</sub>	0.701			OOH* $\longrightarrow$ O <sub>2</sub> <sup>+</sup> H <sup>+</sup>
Cd <sub>6</sub> (CoO <sub>3</sub> ) <sub>5</sub>	0.391			H <sub>2</sub> O <sup>+</sup> O* $\longrightarrow$ OOH <sup>++</sup> H <sup>+</sup>
Ag <sub>2</sub> SeO <sub>3</sub>	0.288	0.192 <sup>88</sup>	0.806	H <sub>2</sub> O <sup>+</sup> O* $\longrightarrow$ OOH <sup>++</sup> H <sup>+</sup>
BaSe <sub>2</sub> O <sub>5</sub>	0.661			H <sub>2</sub> O <sup>+</sup> O* $\longrightarrow$ OOH <sup>++</sup> H <sup>+</sup>
LuCoO <sub>3</sub>	0.559			OOH* $\longrightarrow$ O <sub>2</sub> <sup>+</sup> H <sup>+</sup>
Ag <sub>4</sub> GeO <sub>4</sub>	0.524			OH $\longrightarrow$ O <sup>++</sup> H <sup>+</sup>
CuReO <sub>4</sub>	0.332			OH $\longrightarrow$ O <sup>++</sup> H <sup>+</sup>
Co <sub>11</sub> CuO <sub>16</sub>	0.564	0.606 <sup>106</sup>		OH $\longrightarrow$ O <sup>++</sup> H <sup>+</sup>
CoSe <sub>2</sub> O <sub>5</sub>	0.400			H <sub>2</sub> O <sup>+</sup> O* $\longrightarrow$ OOH <sup>++</sup> H <sup>+</sup>
Co <sub>5</sub> SbO <sub>8</sub>	0.486	<sup>72</sup>		OH $\longrightarrow$ O <sup>++</sup> H <sup>+</sup>
NaTlO <sub>2</sub>	0.489			OH $\longrightarrow$ O <sup>++</sup> H <sup>+</sup>
MgIn <sub>2</sub> O <sub>4</sub>	0.417			H <sub>2</sub> O <sup>+</sup> O* $\longrightarrow$ OOH <sup>++</sup> H <sup>+</sup>
Li <sub>7</sub> Co <sub>5</sub> O <sub>12</sub>	0.381	0.430 <sup>89</sup>		OH $\longrightarrow$ O <sup>++</sup> H <sup>+</sup>
Hg <sub>2</sub> WO <sub>4</sub>	0.679			H <sub>2</sub> O <sup>+</sup> O* $\longrightarrow$ OOH <sup>++</sup> H <sup>+</sup>
CuReO <sub>4</sub>	0.555			OH $\longrightarrow$ O <sup>++</sup> H <sup>+</sup>
Sn <sub>2</sub> Ge <sub>2</sub> O <sub>7</sub>	0.552			H <sub>2</sub> O <sup>+</sup> O* $\longrightarrow$ OOH <sup>++</sup> H <sup>+</sup>
MnTlO <sub>3</sub>	0.196		0.080	H <sub>2</sub> O <sup>+</sup> O* $\longrightarrow$ OOH <sup>++</sup> H <sup>+</sup>

Table 14: Overpotentials from OC22, the experimental literature, and DFT (see Figure 7(b) in the main manuscript) along with the PDS for our final set of 190 candidate (continued).

Formula	$\eta$ (V) (OC22)	$\eta$ (V) (exp.)	$\eta$ (V) (DFT)	PDS
$\text{Ag}_2\text{HgO}_2$	0.473			$\text{OH} \longrightarrow \text{O}^{*+}\text{H}^+$
$\text{Co}_2\text{NiO}_4$	0.504	0.390, <sup>107</sup> 0.316-0.438 <sup>108</sup>		$\text{OH} \longrightarrow \text{O}^{*+}\text{H}^+$
$\text{Ba}_8(\text{Bi}_2\text{O}_7)_3$	0.464			$\text{OH} \longrightarrow \text{O}^{*+}\text{H}^+$
$\text{AgSbO}_4$	0.319			$\text{OOH}^* \longrightarrow \text{O}_2^+\text{H}^+$
$\text{MnTlO}_3$	0.359			$\text{OH} \longrightarrow \text{O}^{*+}\text{H}^+$
$\text{Ca}(\text{CoO}_2)_2$	0.321	0.331 <sup>109</sup>		$\text{H}_2\text{O}^+\text{O}^* \longrightarrow \text{OOH}^{*+}\text{H}^+$
$\text{Tl}_2\text{SeO}_4$	0.577			$\text{OH} \longrightarrow \text{O}^{*+}\text{H}^+$
$\text{Tl}_2\text{SeO}_4$	0.520			$\text{OH} \longrightarrow \text{O}^{*+}\text{H}^+$
$\text{CaSeO}_3$	0.603			$\text{OH} \longrightarrow \text{O}^{*+}\text{H}^+$
$\text{CdCu}_2\text{O}_3$	0.495			$\text{OH} \longrightarrow \text{O}^{*+}\text{H}^+$
$\text{CuSbO}_4$	0.364			$\text{OH} \longrightarrow \text{O}^{*+}\text{H}^+$
$\text{YMn}_2\text{O}_5$	0.540			$\text{OH} \longrightarrow \text{O}^{*+}\text{H}^+$
$\text{Cu}_2\text{W}_2\text{O}_7$	0.425	0.270 <sup>93</sup>		$\text{OH} \longrightarrow \text{O}^{*+}\text{H}^+$
$\text{Ca}_3\text{WO}_6$	0.488			$\text{H}_2\text{O} \longrightarrow \text{OH}\cdot^+\text{H}^+$
$\text{YCoO}_3$	0.517			$\text{OH} \longrightarrow \text{O}^{*+}\text{H}^+$
$\text{ZnCu}_2\text{O}_3$	0.423	0.550 <sup>110</sup>		$\text{OH} \longrightarrow \text{O}^{*+}\text{H}^+$
$\text{CuNiO}_2$	0.401	0.580 <sup>111</sup>		$\text{H}_2\text{O}^+\text{O}^* \longrightarrow \text{OOH}^{*+}\text{H}^+$
$\text{MnBiO}_3$	0.509			$\text{OH} \longrightarrow \text{O}^{*+}\text{H}^+$

Table 15: Overpotentials from OC22, the experimental literature, and DFT (see Figure 7(b) in the main manuscript) along with the PDS for our final set of 190 candidate (continued). All materials listed from here are unstable as bulk materials ( $E_{PBX} > 0.5$  eV) but can be stabilized as nanoparticles.

Formula	$\eta$ (V) (OC22)	$\eta$ (V) (exp.)	$\eta$ (V) (DFT)	PDS
Cr <sub>2</sub> WO <sub>6</sub>	0.252			OOH* $\longrightarrow$ O <sub>2</sub> <sup>+</sup> H <sup>+</sup>
TlCuO <sub>2</sub>	0.426			OH $\longrightarrow$ O <sup>+</sup> H <sup>+</sup>
Y(FeO <sub>2</sub> ) <sub>2</sub>	0.534	0.214 <sup>112</sup>		H <sub>2</sub> O <sup>+</sup> O* $\longrightarrow$ OOH <sup>+</sup> H <sup>+</sup>
Sr <sub>2</sub> Tl <sub>2</sub> O <sub>5</sub>	0.374			OOH* $\longrightarrow$ O <sub>2</sub> <sup>+</sup> H <sup>+</sup>
ZrCoO <sub>3</sub>	0.458	0.400 <sup>113</sup>		OH $\longrightarrow$ O <sup>+</sup> H <sup>+</sup>
TiVO <sub>4</sub>	0.584			H <sub>2</sub> O <sup>+</sup> O* $\longrightarrow$ OOH <sup>+</sup> H <sup>+</sup>
HfFeO <sub>3</sub>	0.529			OOH* $\longrightarrow$ O <sub>2</sub> <sup>+</sup> H <sup>+</sup>
Mn <sub>4</sub> CuO <sub>8</sub>	0.386	0.150 <sup>114</sup>		OH $\longrightarrow$ O <sup>+</sup> H <sup>+</sup>
CoCu <sub>2</sub> O <sub>3</sub>	0.417	0.606 <sup>106</sup>		H <sub>2</sub> O <sup>+</sup> O* $\longrightarrow$ OOH <sup>+</sup> H <sup>+</sup>
MnSe <sub>2</sub> O <sub>5</sub>	0.495			OH $\longrightarrow$ O <sup>+</sup> H <sup>+</sup>
CrMoO <sub>4</sub>	0.416			OH $\longrightarrow$ O <sup>+</sup> H <sup>+</sup>
KMn <sub>2</sub> O <sub>4</sub>	0.470			H <sub>2</sub> O <sup>+</sup> O* $\longrightarrow$ OOH <sup>+</sup> H <sup>+</sup>
Ba <sub>2</sub> Tl <sub>2</sub> O <sub>5</sub>	0.336			OH $\longrightarrow$ O <sup>+</sup> H <sup>+</sup>
LuMnO <sub>3</sub>	0.544			OH $\longrightarrow$ O <sup>+</sup> H <sup>+</sup>
TiMnO <sub>3</sub>	0.279	0.400 <sup>115</sup>	0.559	OH $\longrightarrow$ O <sup>+</sup> H <sup>+</sup>
KBiO <sub>2</sub>	0.267		0.278	H <sub>2</sub> O $\longrightarrow$ OH· <sup>+</sup> H <sup>+</sup>
Na <sub>5</sub> ReO <sub>6</sub>	0.298		0.965	OH $\longrightarrow$ O <sup>+</sup> H <sup>+</sup>
CuTeO <sub>4</sub>	0.537			OH $\longrightarrow$ O <sup>+</sup> H <sup>+</sup>
ScCrO <sub>3</sub>	0.458			H <sub>2</sub> O <sup>+</sup> O* $\longrightarrow$ OOH <sup>+</sup> H <sup>+</sup>
Ta <sub>2</sub> CrO <sub>6</sub>	0.557			OOH* $\longrightarrow$ O <sub>2</sub> <sup>+</sup> H <sup>+</sup>
MnSnO <sub>3</sub>	0.428			OH $\longrightarrow$ O <sup>+</sup> H <sup>+</sup>
Li <sub>4</sub> PbO <sub>4</sub>	0.661			H <sub>2</sub> O $\longrightarrow$ OH· <sup>+</sup> H <sup>+</sup>
VSbO <sub>4</sub>	0.436			OOH* $\longrightarrow$ O <sub>2</sub> <sup>+</sup> H <sup>+</sup>
ScCuO <sub>2</sub>	0.407			H <sub>2</sub> O <sup>+</sup> O* $\longrightarrow$ OOH <sup>+</sup> H <sup>+</sup>
Mn <sub>2</sub> BeO <sub>4</sub>	0.324			OOH* $\longrightarrow$ O <sub>2</sub> <sup>+</sup> H <sup>+</sup>
AlCuO <sub>2</sub>	0.479			H <sub>2</sub> O <sup>+</sup> O* $\longrightarrow$ OOH <sup>+</sup> H <sup>+</sup>
TiCu <sub>3</sub> O <sub>4</sub>	0.375			H <sub>2</sub> O <sup>+</sup> O* $\longrightarrow$ OOH <sup>+</sup> H <sup>+</sup>
Ag <sub>2</sub> PbO <sub>2</sub>	0.434			H <sub>2</sub> O <sup>+</sup> O* $\longrightarrow$ OOH <sup>+</sup> H <sup>+</sup>
LuCrO <sub>3</sub>	0.435			OH $\longrightarrow$ O <sup>+</sup> H <sup>+</sup>
VSeO <sub>4</sub>	0.458			OH $\longrightarrow$ O <sup>+</sup> H <sup>+</sup>
Ag <sub>3</sub> RuO <sub>4</sub>	0.601			H <sub>2</sub> O <sup>+</sup> O* $\longrightarrow$ OOH <sup>+</sup> H <sup>+</sup>
GePb <sub>5</sub> O <sub>7</sub>	0.684			OH $\longrightarrow$ O <sup>+</sup> H <sup>+</sup>
VCrO <sub>4</sub>	0.320			OOH* $\longrightarrow$ O <sub>2</sub> <sup>+</sup> H <sup>+</sup>
TlTeO <sub>4</sub>	0.496			H <sub>2</sub> O $\longrightarrow$ OH· <sup>+</sup> H <sup>+</sup>
MnSeO <sub>3</sub>	0.438			OH $\longrightarrow$ O <sup>+</sup> H <sup>+</sup>

Table 16: Overpotentials from OC22, the experimental literature, and DFT (see Figure 7(b) in the main manuscript) along with the PDS for our final set of 190 candidate (continued).

Formula	$\eta$ (V) (OC22)	$\eta$ (V) (exp.)	$\eta$ (V) (DFT)	PDS
Li <sub>3</sub> BiO <sub>3</sub>	0.523			OH $\longrightarrow$ O <sup>*+</sup> H <sup>+</sup>
VZn <sub>2</sub> O <sub>4</sub>	0.474			H <sub>2</sub> O <sup>+</sup> O <sup>*</sup> $\longrightarrow$ OOH <sup>*+</sup> H <sup>+</sup>
Fe <sub>10</sub> O <sub>11</sub>	0.499	0.449 <sup>76</sup>		H <sub>2</sub> O <sup>+</sup> O <sup>*</sup> $\longrightarrow$ OOH <sup>*+</sup> H <sup>+</sup>
Tl <sub>2</sub> SnO <sub>3</sub>	0.596			H <sub>2</sub> O <sup>+</sup> O <sup>*</sup> $\longrightarrow$ OOH <sup>*+</sup> H <sup>+</sup>
ScMn <sub>2</sub> O <sub>4</sub>	0.285		0.328	OH $\longrightarrow$ O <sup>*+</sup> H <sup>+</sup>
ZrMnO <sub>3</sub>	0.501			H <sub>2</sub> O <sup>+</sup> O <sup>*</sup> $\longrightarrow$ OOH <sup>*+</sup> H <sup>+</sup>
Li(CuO) <sub>2</sub>	0.515			OOH <sup>*</sup> $\longrightarrow$ O <sub>2</sub> <sup>+</sup> H <sup>+</sup>
Fe <sub>17</sub> O <sub>18</sub>	0.524	0.449 <sup>76</sup>		OH $\longrightarrow$ O <sup>*+</sup> H <sup>+</sup>
K <sub>6</sub> Co <sub>2</sub> O <sub>7</sub>	0.360			OH $\longrightarrow$ O <sup>*+</sup> H <sup>+</sup>
Cr <sub>2</sub> NiO <sub>4</sub>	0.381	0.334 <sup>116</sup>		H <sub>2</sub> O <sup>+</sup> O <sup>*</sup> $\longrightarrow$ OOH <sup>*+</sup> H <sup>+</sup>
YCuO <sub>2</sub>	0.380			H <sub>2</sub> O <sup>+</sup> O <sup>*</sup> $\longrightarrow$ OOH <sup>*+</sup> H <sup>+</sup>
Mn <sub>2</sub> SnO <sub>4</sub>	0.425			OH $\longrightarrow$ O <sup>*+</sup> H <sup>+</sup>
MnCuO <sub>2</sub>	0.577	0.150 <sup>114</sup>		H <sub>2</sub> O <sup>+</sup> O <sup>*</sup> $\longrightarrow$ OOH <sup>*+</sup> H <sup>+</sup>
YCuO <sub>2</sub>	0.377			OH $\longrightarrow$ O <sup>*+</sup> H <sup>+</sup>
Mn <sub>23</sub> FeO <sub>32</sub>	0.280	0.47 <sup>75</sup>	0.291	OH $\longrightarrow$ O <sup>*+</sup> H <sup>+</sup>
SrCr <sub>2</sub> O <sub>4</sub>	0.623			H <sub>2</sub> O <sup>+</sup> O <sup>*</sup> $\longrightarrow$ OOH <sup>*+</sup> H <sup>+</sup>
KSnO <sub>2</sub>	0.194		1.314	OH $\longrightarrow$ O <sup>*+</sup> H <sup>+</sup>
CdRuO <sub>4</sub>	0.530	0.266 <sup>117</sup>		OOH <sup>*</sup> $\longrightarrow$ O <sub>2</sub> <sup>+</sup> H <sup>+</sup>
Co(SbO <sub>2</sub> ) <sub>2</sub>	0.660	<sup>72</sup>		OOH <sup>*</sup> $\longrightarrow$ O <sub>2</sub> <sup>+</sup> H <sup>+</sup>
Mn <sub>2</sub> CrO <sub>4</sub>	0.371	0.367 <sup>118</sup>		H <sub>2</sub> O <sup>+</sup> O <sup>*</sup> $\longrightarrow$ OOH <sup>*+</sup> H <sup>+</sup>
Na <sub>2</sub> Sb <sub>4</sub> O <sub>7</sub>	0.355			OH $\longrightarrow$ O <sup>*+</sup> H <sup>+</sup>
CeCrO <sub>3</sub>	0.293			H <sub>2</sub> O <sup>+</sup> O <sup>*</sup> $\longrightarrow$ OOH <sup>*+</sup> H <sup>+</sup>
Na <sub>2</sub> Co <sub>2</sub> O <sub>3</sub>	0.297	0.236 <sup>83</sup>	0.288	OH $\longrightarrow$ O <sup>*+</sup> H <sup>+</sup>
NaSb <sub>5</sub> O <sub>8</sub>	0.517			H <sub>2</sub> O <sup>+</sup> O <sup>*</sup> $\longrightarrow$ OOH <sup>*+</sup> H <sup>+</sup>
RuPbO <sub>4</sub>	0.640			OH $\longrightarrow$ O <sup>*+</sup> H <sup>+</sup>
SnRuO <sub>4</sub>	0.321			H <sub>2</sub> O <sup>+</sup> O <sup>*</sup> $\longrightarrow$ OOH <sup>*+</sup> H <sup>+</sup>
Ti(SnO <sub>2</sub> ) <sub>2</sub>	0.476			H <sub>2</sub> O <sup>+</sup> O <sup>*</sup> $\longrightarrow$ OOH <sup>*+</sup> H <sup>+</sup>
LiMn <sub>3</sub> O <sub>4</sub>	0.630			OH $\longrightarrow$ O <sup>*+</sup> H <sup>+</sup>
K <sub>2</sub> PbO <sub>2</sub>	0.549			OOH <sup>*</sup> $\longrightarrow$ O <sub>2</sub> <sup>+</sup> H <sup>+</sup>
Mn <sub>2</sub> NiO <sub>3</sub>	0.470			OOH <sup>*</sup> $\longrightarrow$ O <sub>2</sub> <sup>+</sup> H <sup>+</sup>
Mn <sub>3</sub> NiO <sub>4</sub>	0.541			H <sub>2</sub> O <sup>+</sup> O <sup>*</sup> $\longrightarrow$ OOH <sup>*+</sup> H <sup>+</sup>
BaMn <sub>2</sub> O <sub>3</sub>	0.624			OOH <sup>*</sup> $\longrightarrow$ O <sub>2</sub> <sup>+</sup> H <sup>+</sup>
CaMn <sub>7</sub> O <sub>8</sub>	0.484	0.400-0.900 <sup>119</sup>		OH $\longrightarrow$ O <sup>*+</sup> H <sup>+</sup>